

Assessment of Capture of Microplastics from Water Using Hydrocyclone Technique

Kacper Filip Pajuro

Offshore Energy Systems, OES4-5-F23,
Spring Semester 2023

Master Thesis





AALBORG UNIVERSITY

STUDENT REPORT

Title:

Assessment of Capture of Microplastics from Water Using Hydrocyclone Technique

Theme:

Master's Thesis

Project Period:

Spring Semester 2023

Project Group:

OES4-5-F23

Participants:

Kacper Filip Pajuro

Supervisors:

Zhenyu Yang

Page Numbers: 54

Date of Completion:

31st May 2023

Abstract:

This project aims to assess the possibility of capture of microplastics from water using hydrocyclone technology. The analysis was based on the data obtained from the experiment, which was conducted at AAU Esbjerg. In order to obtain information about microplastics concentration in water, dynamic microscopes were installed in the setup. A dedicated calibration procedure, consisting of statistical tests and measures, was proposed to ensure appropriate detection performance of the sensors. Mean efficiencies were obtained for specific sets of control valve settings. The highest observed separation efficiency achieved 87,76%, which can be compared with hydrocyclone performance in other industries. The hydrocyclone can be used for efficient separation of microplastics from water. A control algorithm of hydrocyclone could be designed in the future, based on performed analysis.

Contents

List of Figures	iv
List of Tables	vi
Preface	1
1 Introduction	2
1.1 Plastic Waste Production	2
1.2 Microplastics	2
2 State of the Art	4
2.1 Ongoing Capture Solutions	4
2.2 Hydrocyclone	5
2.3 Problem Formulation	5
3 Setup	7
3.1 ViPA Sensor	7
3.1.1 Area	9
3.1.2 Perimeter	9
3.1.3 Ferets Min and Max	9
3.1.4 Size	9
3.1.5 Shape Factor	10
3.1.6 Estimated Volume	10
3.1.7 Concentration	10
3.2 Setup	10
3.2.1 Calibration Setup	10
3.2.2 Main Experiment Setup	12
4 Calibration	15
4.1 Calibration Parameters	15
4.1.1 Edge Strength	15
4.1.2 Threshold Value	15

4.2	Calibration Procedure	16
4.2.1	Z-test and Number of Particles	19
4.2.2	Kolmogorov-Smirnov Test	21
4.2.3	Chi-square Test	22
4.2.4	KL Divergence	23
4.2.5	JS Divergence	24
4.2.6	Sum of Squared Errors	25
4.2.7	Comparison of Methods	26
4.3	Validation Procedure	27
5	Assessment of Hydrocyclone Separation Capability	32
5.1	Experiment Design	32
5.2	Data Preprocessing	34
5.2.1	ViPA Data Preprocessing	34
5.2.2	Signals Data Preprocessing	35
5.3	Efficiency Results	35
5.3.1	Influence of Q_i and PDR	40
5.3.2	Size Distribution of Microbeads	42
6	Conclusions	44
7	Discussion	45
	Bibliography	47
A	Additional Plots	51

List of Figures

2.1	Hydrocyclone separation principle [16]	5
3.1	Schematic of core components [19]	8
3.2	Focus of particles and DoF	8
3.3	Ferets of a particle	9
3.4	Diagram of the calibration setup	11
3.5	PDF and CDF of BS-Partikel particles, mean diameter: 40,3 μm	11
3.6	PDF and CDF of BS-Partikel particles, mean diameter: 79,4 μm	12
3.7	Diagram of the main experiment setup	12
3.8	Picture of the experiment setup	13
3.9	Plastic microbeads	14
4.1	Particle images for subjective calibration of ViPA-1	16
4.2	Particle images for subjective calibration of ViPA-2	16
4.3	Particle images for subjective calibration of ViPA-2	17
4.4	Experiments with passed z-test and $n > 1000$ for sensor ViPA-1	20
4.5	Experiments with passed z-test and $n > 1000$ for sensor ViPA-2	21
4.6	Visualisation of binning, $P(x)$ and $Q(x)$	24
4.7	Probabilities for ViPA-1, ESV: 3, TV: 64	28
4.8	Probabilities for ViPA-2, ESV: 4, TV: 84	28
4.9	Validation probabilities for ViPA-1, ESV: 3, TV: 64	29
4.10	Validation probabilities for ViPA-2, ESV: 4, TV: 84	29
4.11	Histogram of all detected particles for ViPA-1, ESV: 3, TV: 64	30
4.12	Histogram of all detected particles for ViPA-2, ESV: 4, TV: 84	31
5.1	Operating conditions during the experiment	33
5.2	Concentration during the experiment for initial and best calibration settings	36
5.3	Efficiency during the experiment for initial and best calibration settings	37
5.4	Separation efficiency heatmap for initial calibration settings	38
5.5	Separation efficiency heatmap for best calibration settings	38
5.6	Efficiency and overflow flow rate Q_o	39
5.7	Efficiency vs Q_i and PDR for initial calibration settings	41

5.8	Efficiency vs Q_i and PDR for best calibration settings	41
5.9	Histogram of detected particles for best efficiency and initial calibration settings	42
5.10	Histogram of detected particles for best efficiency and best calibration settings	43
A.1	All valve angles and pump signal	51
A.2	All pressure signals	52
A.3	All flow rate signals	53
A.4	Histogram of all detected particles for initial calibration settings	54
A.5	Histogram of all detected particles for best calibration settings	54

List of Tables

3.1	ViPA sensor key specification [18] [19]	7
4.1	Subjective calibration results for sensor ViPA-1	18
4.2	Subjective calibration results for sensor ViPA-2	18
4.3	Best performing experiments according to d_{KS}	22
4.4	Best performing experiments according to T_{norm}	23
4.5	Best performing experiments according to $D_{KL}(P Q)$	25
4.6	Best performing experiments according to $JSD(P Q)$	25
4.7	Best performing experiments according to SSE	26
4.8	Comparison of the best calibration settings from different methods	26
5.1	Fragment of particle data before addition of empty frames	35
5.2	Fragment of particle data after addition of empty frames	35
5.3	Best performing valve settings according to e	40

Preface

This project was created by Master's student of Offshore Energy Systems at Aalborg University Esbjerg, and was written during the first semester of 2023. The group thanks Zhenyu Yang for supervising this thesis, as well as Aalborg University for the equipment used. The group would also like to thank Dennis Severin Hansen for providing the necessary data for this project and general support.

Aalborg University, 31st May 2023



Kacper Filip Pajuro
<kpajur21@student.aau.dk>

Chapter 1

Introduction

1.1 Plastic Waste Production

Since the invention of plastic, humanity faced the challenge of its recycling. Due to its lightweight, low cost or durability, plastic is widely used in many applications such as packaging, construction or medicine. As plastic is made from polymers, it often takes hundreds of years to decompose naturally. Therefore, the immense demand for its production results in generation of vast amount of waste. It is estimated that throughout 100 years of plastic production, 6,3 Gigatons (Gt) of plastic waste has been generated. Unfortunately, only 9% of it was recycled, while 12% was incinerated and 79% was collected in landfills or directly disposed to natural environment. If more strict policies are not to be implemented, by 2050 around 12 Gt of plastic waste are estimated to be accumulated in the environment or landfills [1].

One of the places where mismanaged plastic waste can be found are oceans. It is assumed that as of 2015, 83 Mt of plastic waste is assembled in oceans worldwide and this amount will increase annually by 8 Mt [2]. This significant volume of plastic causes the extreme phenomenons such as accumulation of floating litter. For example, one of the largest plastic concentration zones Great Pacific Garbage Patch has the area of 1,6 million km², which can be compared to the square area of Mongolia. Moreover, the accumulation of plastic mass accelerates in this zone, which inevitably influences negatively the natural habitat of oceans [3].

1.2 Microplastics

Microplastics are usually defined as plastic particles smaller than 5 mm [4]. Some microplastics are manufactured deliberately to be used, for example in cosmetics. Unfortunately, microplastic can also be a product of undesirable degradation of larger plastic in a marine environment. Waves, currents, heat from sun or even marine life are examples of factors that allows plastic to degrade into smaller pieces. It should be noted

that around 60% of microplastics have lower density than water, thus they float close to the surface. Due to currents occurring in oceans, microplastics may be accumulated in areas such as the Great Pacific Garbage Patch, where microplastics contribute to 94% of all estimated pieces [3].

Due to the small size of microplastic, numerous marine organisms, for example fish, unintentionally consume plastic while eating or breathing [5]. Accumulation of microplastic, especially in lower level organisms, for example zooplankton, may negatively affect their growth or survival [6]. Moreover, microplastic, found in small marine organism, may be transferred to larger animals via the food chain [7]. Furthermore, microplastic can also be accumulated in humans, as its occurrence was observed in human faeces [8]. Microplastic not only enters the human body during consumption, but also while breathing, as even air contains small plastic particles. Although it is evident that humans are prone to assimilation of microplastics, the contribution of microplastics to overall chemical intake is rather small [9]. Moreover, the long-time effects of microplastics on human health seem questionable and more research needs to be conducted [10].

Nevertheless, it is indisputable that microplastics negatively affect the natural environment. One of the paths to reduce the volume of microplastics in marine habitat is more efficient recycling and management of plastic waste. It is necessary to implement new policies to prevent unwanted generation of microplastic volume in the future. However, even if the production of plastic waste is reduced, microplastic will still remain in the marine environment as it takes a long time to decompose. Therefore, this paper will be focused on the capture of microplastics from water. The ongoing technological possibilities of separation of microplastic from water will be presented in Chapter 2.

Chapter 2

State of the Art

2.1 Ongoing Capture Solutions

Due to several factors, the capture of microplastics is a challenging task. Firstly, it can be demanding to even properly detect microplastics. As mentioned in Chapter 1, microplastics vary in size. Additionally, microplastics may differ in composition, shape, or their concentration in water, which further complicates their detection.

One of the most commonly used methods of measuring microplastic concentration in water is a visual detection of particles using microscopy. Generally, there is a risk of incorrect classification of other small particles as microplastics, however microscopes may detect various kinds of microplastics, regardless of their composition [11]. Moreover, additional classification algorithms, for instance machine learning, may be used to improve classification of microplastics, detected through microscopy. Other methods of detection may be used, for example fluorescence-based sensors, however some microplastics may not be detected, due to low or no affinity for fluorescent dye. It should be noted that some detection methods require sample collection and laboratory equipment. Offline sampling methods may generate more precise and sophisticated results, however detection is more time-consuming, and it may be more beneficial for capture purposes to observe concentration of particles in real-time.

Currently, numerous technologies of microplastic capture from water are being implemented and developed. A filter-based approach can be used in wastewater treatment plants (WWTP) to separate microplastics from water, along with other small particles. Glass, membrane or other filters may be straightforwardly applied in WWTPs for microplastic separation processes [12]. However, small particles may not be captured in certain filters and the risk of frequent filter clogging can be considered as drawbacks in this technology [13].

Another technological approach of microplastic capture is the use of electrocoagulation. It is a process that removes contaminants from water using anode, cathode and direct current. More efficient separation performance was observed with comparison

to filtration. On the other hand, this process requires additional energy input and thus economy of this process should be further investigated, along with design of specific reactor [14].

Additionally, there are also some chemical methods of microplastic capture. Chemical coagulation may simplify separation of particles from water. However, addition of chemicals to water may not be considered beneficial and observed separation efficiency is lower than in aforementioned methods [15].

2.2 Hydrocyclone

In principle, hydrocyclone is a device which separates fluids or solids from other fluids, based on density differences in a mixture. Figure 2.1 presents a diagram of hydrocyclone and its principle. It consists of at least one tangential inlet, through which a mixture of fluids enters the cylinder. Due to its conical shape, it creates a vortex that separates due to centripetal force. The lighter phase (marked in black) moves towards the centre of the cylinder, creating a vortex core which exits the cylinder through the overflow outlet. The heavier phase (marked in gray) is forced towards the wall and exits the hydrocyclone on the other side, through the underflow outlet. Sometimes, multiple hydrocyclones are used parallelly to handle large volume of heavier fluid. Hydrocyclones perform separation of phases in various applications, for instance in the oil industry, where they remove oil from water. There are several key advantages of this separation device, such as relatively high efficiency of separation, lack of moving parts and cost-efficiency [16].

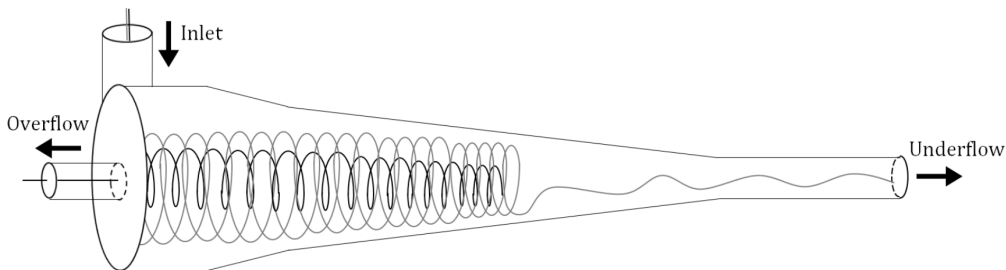


Figure 2.1: Hydrocyclone separation principle [16]

2.3 Problem Formulation

In conclusion, despite challenges related to appropriate measuring of microplastic concentration in water, numerous technologies are being implemented or developed to remove microplastics from water. Unfortunately, none of them can be considered as optimal or perfect option, due to drawbacks associated with lower separation efficiency,

filter clogging, time-consuming or expensive solutions, as well as separation dependency on chemical properties of observed particles.

This project aims to overcome some of these disadvantages by implementation of hydrocyclone in the process of microplastic capture. In accordance with its principle described in Section 2.2, the mixture of water and microplastic could enter the hydrocyclone through the inlet. After separation in the cylinder, ideally, clean water would exit the hydrocyclone through the underflow valve and a more concentrated mixture of microplastic and water would enter hydrocyclone through the overflow valve. It should be noted that this would occur under the assumption that observed microplastic has lower density than water. Potentially, hydrocyclone could be used together with already existing technology of microplastic separation, for example before a dead-end filtration unit. As hydrocyclone could possibly remove up to 90% of microplastic particles [17], the problem of frequent replacement of filters would be significantly reduced.

Therefore, the following problem statement was formulated:

Can hydrocyclone be used for efficient separation of microplastics from water, and how to determine its separation efficiency with a dynamic microscope?

In order to answer the above problem question, the setup with a hydrocyclone, located in the Offshore Laboratory at AAU, will be used. The description of the setup can be found in Chapter 3. The calibration procedure of used microscopy sensors will be described in Chapter 4, whereas the assessment of hydrocyclone separation capabilities will be presented in Chapter 5.

Chapter 3

Setup

This chapter contains description of sensors used for detection of microplastic in the water. In order to further visualize the equipment used for this project, all versions of setup are described.

3.1 ViPA Sensor

The sensor that was used in this project to detect microplastics in water is the Visual Process Analyzer (ViPA), manufactured by Jorin. This dynamic microscope is not limited to recognition of only solid particles in a mixture, as it can also identify bubbles or droplets. Its key properties are presented in Table 3.1.

Particle size range	1,2-150 μm
Concentration	0-2500 ppmV
Length of a pixel	0.375
Inlet and outlet ports	1/4"
Flow rate	up to 4 l/min
Max operating pressure	120 bar
Frame rate	\sim 30 fps
Pixel length conversion factor	0.375 $\mu\text{m}/\text{pixel}$
Pixel area conversion factor	0.1406 $\mu\text{m}^2/\text{pixel}$

Table 3.1: ViPA sensor key specification [18] [19]

ViPA sensor detects particles through microscopy. The main measuring unit contains a high speed digital video camera on the one side of a flow cell, and a light source on the other side. In Figure 3.1, it can be observed that the camera detects particles not in the whole width of the view cell, but only in the specific length called Depth of Field (DoF). Microplastics and other elements, which flow outside DoF, are determined as out

of focus and are rejected. The example of such phenomenon can be observed in Figure 3.2. It is evident that location of a particle significantly contributes to its focus.

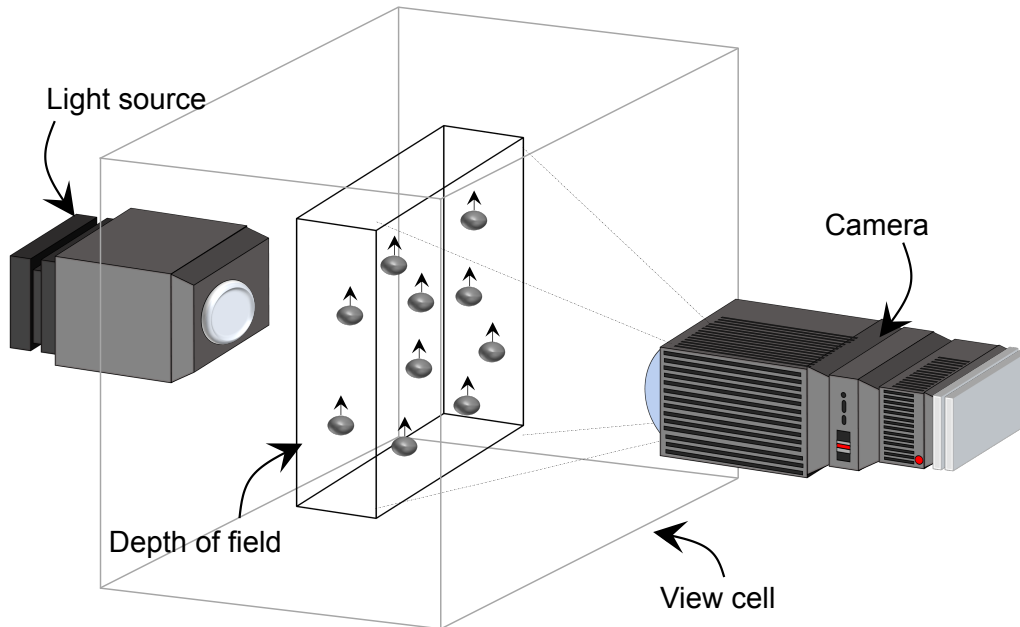


Figure 3.1: Schematic of core components [19]

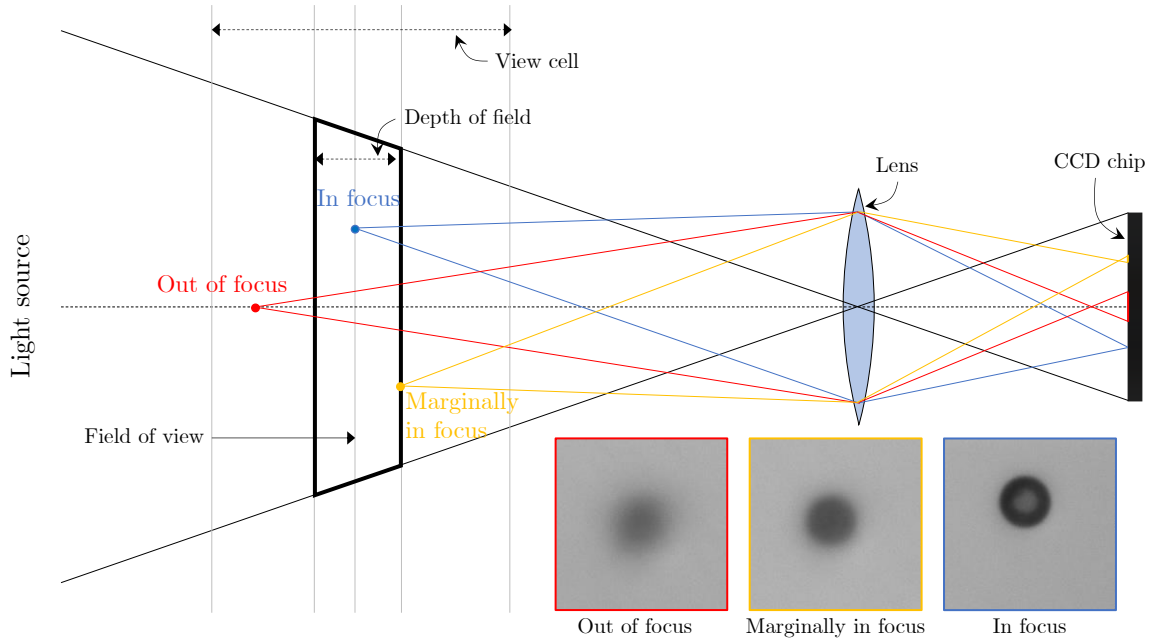


Figure 3.2: Focus of particles and DoF

Information obtained through the microscope is transferred to the computer via fibre-optic cable. Then, dedicated ViPA software performs image processing on pictures with detected particles. Meaningful particle data is then obtained, with 36 parameters providing information about the detected particle. The most relevant parameters are described below [18].

3.1.1 Area

In order to obtain information about area of a detected particle, ViPA software counts the number of pixels inside a particle and then multiplies it by the fixed area conversion factor. The calculated area is in μm^2 .

3.1.2 Perimeter

ViPA software counts the number of pixels that are creating the edge of a particle. This number is then multiplied by the fixed length conversion factor, to obtain the perimeter in μm .

3.1.3 Ferets Min and Max

Feret is defined by ViPA software as a distance between 2 sides of a particle edge, calculated at a specific axis. 4 ferets are calculated, and their axis are presented in Figure 3.3. The shortest and the longest distance are provided via ViPA software as Feret min and Feret max.

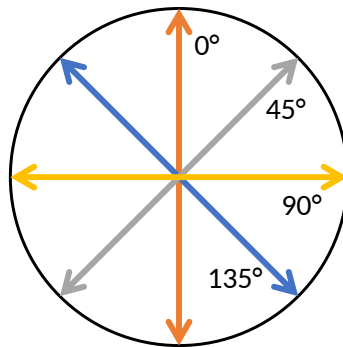


Figure 3.3: Ferets of a particle

3.1.4 Size

The size of a particle is calculated as an average of four ferets.

3.1.5 Shape Factor

Shape factor provides information on how spherical a particle is. The value of shape factor is in a range between 0 and 1, and it is calculated based on Equation 3.1. The particle which is observed as a perfect circle will have a shape factor of 1, whereas particles which are less spherical will have values closer to 0.

$$\text{Shape factor} = \frac{4\pi \text{Area}}{\text{Perimeter}^2} \quad (3.1)$$

3.1.6 Estimated Volume

The size of a particle is calculated in a manner that it is assumed to be a diameter of a spherical particle. Therefore, the estimated volume is calculated using the formula for the volume of a sphere, which is presented in Figure 3.2.

$$\text{Volume} = \frac{\text{Size}^3 \pi}{6} \quad (3.2)$$

3.1.7 Concentration

ViPA software provides information about the concentration for each frame with detected particle. In order to calculate the concentration, the volume of passing mixture is obtained by multiplication of frame area by DoF. Then, the concentration is derived by dividing the sum of estimated volumes of particles in the frame, by the volume of passing mixture. Obtained frame concentration is provided in Visible parts per million (Vppm).

The frame concentration should not be considered as absolute, because particles which flow outside DoF are not in focus, thus they are disregarded. It should be noted that in order to properly calculate concentration, the flow rate of fluid must be higher than the frame rate, to ensure that in every frame, the new volume is analysed. However, this condition is met for all conducted experiments.

3.2 Setup

3.2.1 Calibration Setup

The setup presented in Figure 3.4 was used for calibration of 2 ViPA sensors. In the calibration loop flows a mixture of demineralized water and calibration particles provided by manufacturer BS-Partikel. One of the characteristics of these particles, is that they are narrowly distributed in size, which can be observed in Figures 3.5 and 3.6, where probability density functions (PDF) and cumulative distribution functions are presented (CDF). Based on this information from the manufacturer, sensors were calibrated with

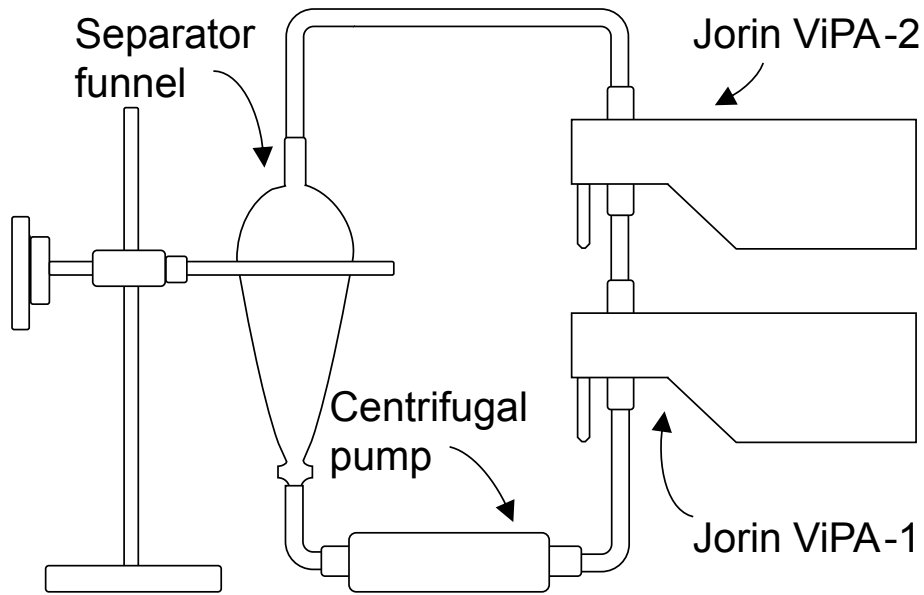


Figure 3.4: Diagram of the calibration setup

particles with mean diameter of $40,3 \mu\text{m}$ and further calibration was validated by addition of particles with larger diameter of $79,4 \mu\text{m}$ to the same loop. This procedure is described in depth in Chapter 4.

The calibration setup also consists of the centrifugal pump, which provides constant flow of mixture in the loop. Additionally, the setup was equipped with the separator funnel, to reduce the problem of particles sticking together.

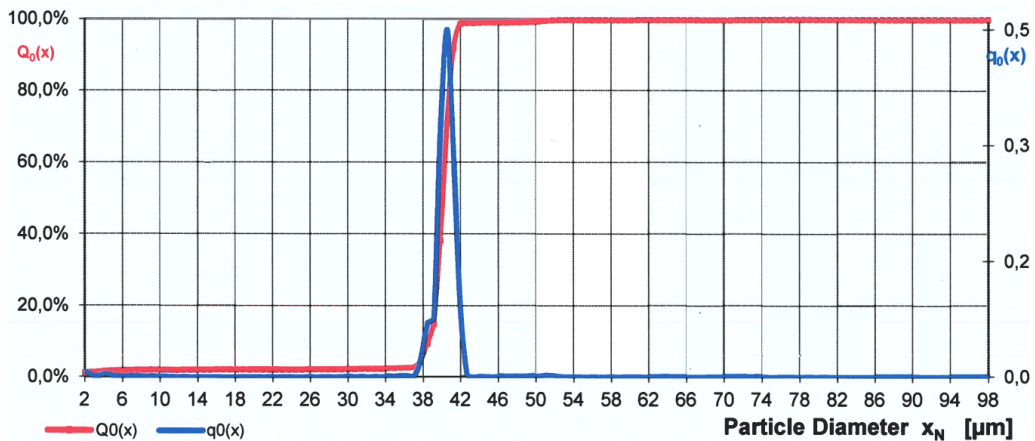


Figure 3.5: PDF and CDF of BS-Partikel particles, mean diameter: $40,3 \mu\text{m}$

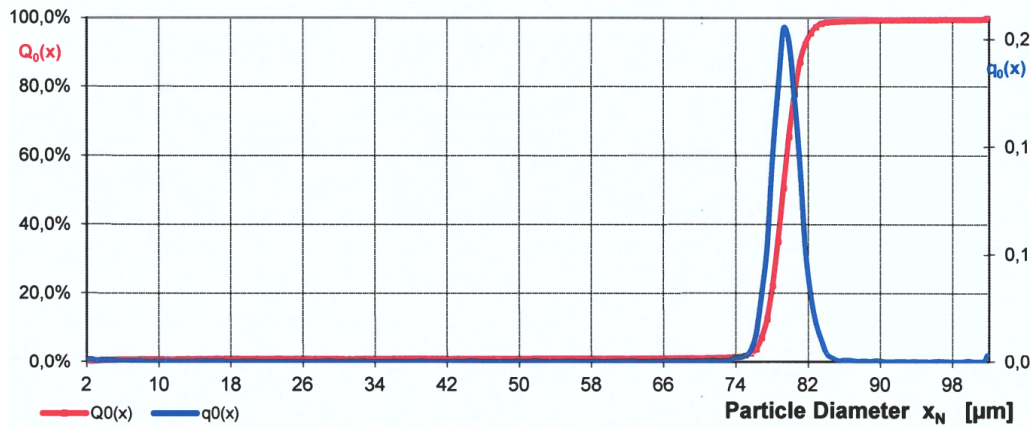


Figure 3.6: PDF and CDF of BS-Partikel particles, mean diameter: 79,4 μm

3.2.2 Main Experiment Setup

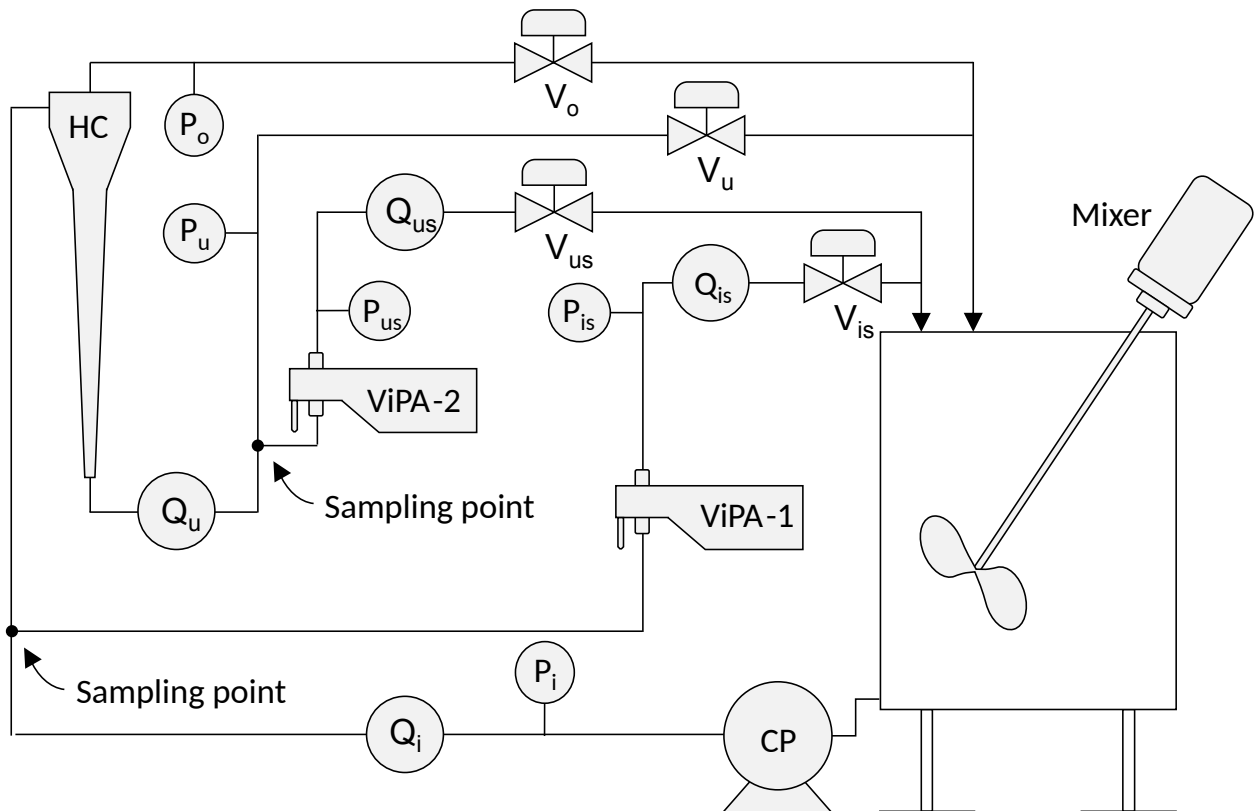


Figure 3.7: Diagram of the main experiment setup

For the main experiment, during which assessment of the hydrocyclone separation



Figure 3.8: Picture of the experiment setup

capability was conducted, the other setup was constructed. Its diagram is presented in Figure 3.7. In order to further visualise the setup, its picture was taken and presented in Figure 3.8.

The setup loop can be divided into 5 parts:

- i - inlet part,
- u - underflow part,
- o - overflow part,
- us - underflow sidestream part,
- os - overflow sidestream part.

Indexes of all elements indicate where in the setup the component is located.

The fluid which flows in this a setup is a mixture of water and a microbeads. These plastic particles differ from BS-Partikel as they are less spherical, and they vary more in size. Red microbeads are visible inside bottles in Figure 3.9. In total, 50g of microbeads were added to the setup. 4 bottles with microbeads size in a range between 53 and 63



Figure 3.9: Plastic microbeads

μm , and 1 bottle with size in a range between 75 and 90 μm were used. The centrifugal pump (CP) ensures the circulation of the mixture in the system.

Due to their design, ViPA sensors perform on-line analysis. Therefore, dedicated sidestreams were introduced in the setup. Sensor ViPA-1 measures particles in the inlet sidestream, whereas sensor ViPA-2 measures particles in the underflow sidestream. Hence, information about concentration can be obtained before and after separation in the hydrocyclone (HC), and consequently efficiency of the process may be calculated. It should be mentioned that in this setup, sidestreams are connected with the main stream via t-junction. There is a risk that sampling in the sidestream may not reflect the true process concentration occurring in the main stream [20].

In order to operate the system and manipulate individual flow rates, control valves V were installed in the system. Additionally, pressure sensors P and flow meters Q were implemented in the setup, in order to provide more information about the process. The separated mixture returns to the tank, where it is amalgamated again using the mixer. The activity of mixing aims to prevent additional separation of microbeads from water inside the tank.

The design of the main experiment, along with the description of operating conditions, are described in Chapter 5.

Chapter 4

Calibration

The purpose of calibration procedure is to ensure that microscopy sensors applied in the setup may reliably detect particles and their sizes. In this chapter, the approach behind calibration procedure will be described. Moreover, the validation of calibration settings was performed, and it will be presented as well.

4.1 Calibration Parameters

Each of the microscopes, described in Chapter 3, consists of 2 selectable parameters, which are influencing capability of detecting particles and their sizes in the system.

4.1.1 Edge Strength

The edge strength of a detected particle may be defined as the rate of change in grey scale from the background at its edges. Thus, the sharper an object seems to be on a picture, the higher edge strength it possesses. Alternatively, if a particle appears blurry in the picture, it may suggest a lower edge strength value (ESV). The method behind detecting the edge of a particle is not provided by the manufacturer of the sensor, however it is assumed that some version of a Sobel filter is applied. The microscope's software allows for the user to select a minimum value of ESV. All particles with lower ESV than selected are disregarded. The possible range of ESV to select is from 0 to 10.

4.1.2 Threshold Value

The threshold value (TV) is the second selectable parameter, and it indicates how dark a particle needs to be with respect to the fixed background in order to classify it as a detected object. The higher the TV is, the darker a particle needs to be in order to detect it. Alternatively, if a selected value of TV is lower, whiter particles are also recognized. The possible range of TV to select is from 0 to 255.

4.2 Calibration Procedure

In order to calibrate microscopes, artificial microplastic particles produced by BS-Partikel were added to the calibration setup, which is described in Section 3.2.1. According to the manufacturer, particles used for calibration follow a normal distribution with the mean size of $40,3 \mu\text{m}$ and standard deviation of $0,89 \mu\text{m}$, which is presented in Figure 3.5.

With respect to the calibration of sensors, the manufacturer provides limited instructions in the manual. It is recommended to select ESV of 2 as a rule of thumb. In addition, manufacturer suggests to tune TV based on a couple of pictures with detected particles.

Based on these instructions, 9 engineers at AAU were asked for assistance with manual calibration of ViPA sensors, by acting as operators. They were provided with BS-Partikel data regarding particle size distribution and with the description of ESV and TV from the manual. Then, they were allowed to adjust calibration parameters based only on 3 images for each sensor. These images are presented in Figures 4.1 and 4.2. The pictures were selected to cover different scenarios of number of particles on the frame and their focus.

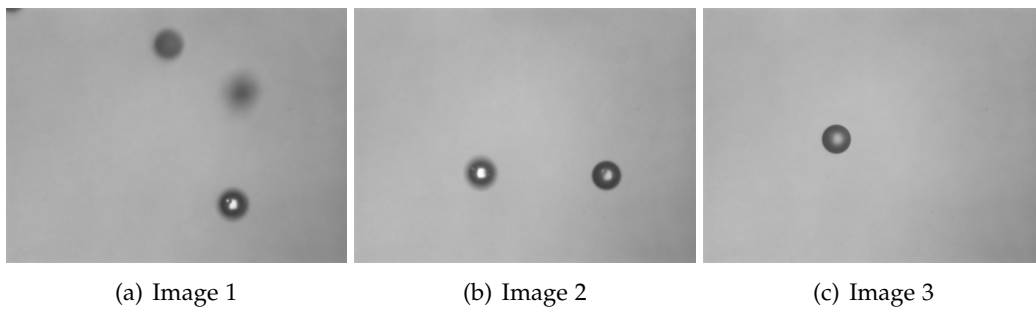


Figure 4.1: Particle images for subjective calibration of ViPA-1

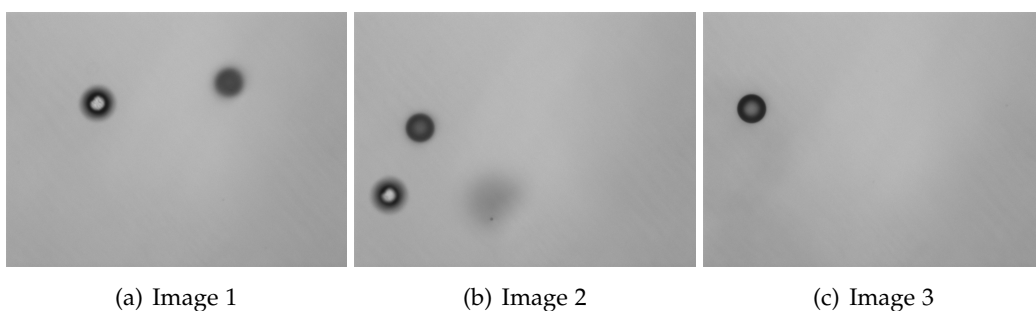


Figure 4.2: Particle images for subjective calibration of ViPA-2

After selection of specific ESV and TV, ViPA software displays the number of detec-

ted particles on the picture and their corresponding size. Additionally, the detected edge of a particle is visualized by a white contour. When ESV and TV are adjusted, particles data and their edges are updated. This is presented in Figure 4.3. Therefore, operators may select specific ESV and TV according to their apprehension of appropriate particle edge and size.

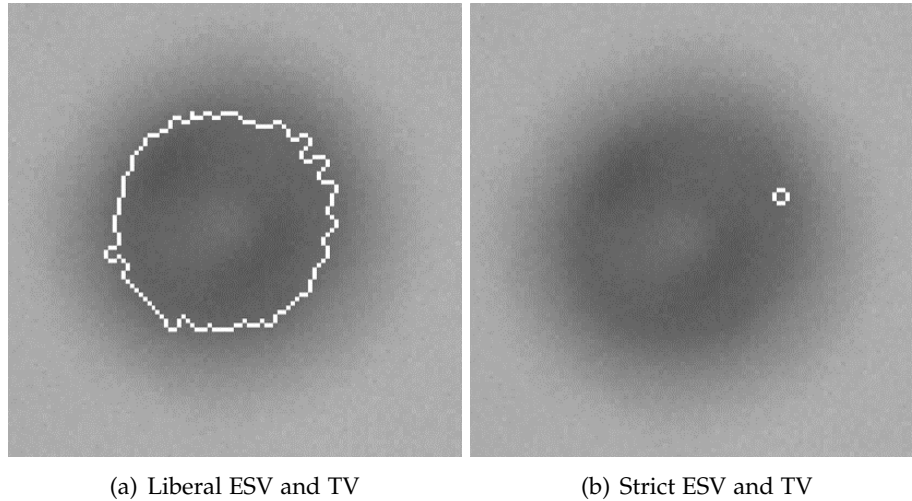


Figure 4.3: Particle images for subjective calibration of ViPA-2

Operators selected calibration settings for every image and every sensor. For every selection, ViPA software computed analysis based on pictures obtained from the experiment, which will be further explained below. Thus, for every selected set of ESV and TV by operators, the mean size of detected particles from the setup was obtained. Additionally, for each image, average ESV and TV were found, based on selections from 9 operators. Thus, the mean size of detected particles was obtained according to a specific image. Moreover, average ESV and TV were found for each of individual operators, based on their selections from 3 images. Thus, the mean size of particles was obtained according to a specific operator. Ultimately, the total average ESV and TV were obtained based on selections from all pictures and operators, and the final total mean of detected particles was calculated. It should be indicated that obtained average calibration settings were rounded to the nearest integer.

Tables 4.1 and 4.2 present obtained results for sensors ViPA-1 and ViPA-2 respectively. It is evident that the selection of appropriate ESV and TV is subjective to operators. Moreover, their choice of calibration parameters differs from image to image.

Obtained total average ESV and TV, proposed mean particle sizes of 43,12 and 41,14 μm , which significantly differ from the true mean size of 40,3 μm , as the standard deviation of true distribution equals 0,89 μm . This indicates, that the calibration procedure cannot be conducted simply by visual inspection of a couple of images, and more ex-

Person	Image 1			Image 2			Image 3			Person mean		
	ESV	TV	Size	ESV	TV	Size	ESV	TV	Size	ESV	TV	Size
1	2	18	44,93	3	46	41,83	2	49	41,66	2	38	43,01
2	3	50	41,47	3	50	41,47	0	30	43,48	2	43	42,33
3	2	18	44,93	4	48	41,63	2	49	41,66	3	38	42,88
4	2	17	44,58	2	55	40,90	2	39	42,68	2	37	42,88
5	2	17	44,58	2	45	42,10	2	49	41,66	2	37	42,88
6	1	15	1,80*	2	18	44,93	2	40	42,68	2	24	44,39
7	2	18	44,93	2	33	43,35	4	49	41,58	3	33	43,09
8	2	21	44,70	2	41	42,50	3	39	42,75	2	34	43,32
9	2	22	44,80	6	48	41,51	2	48	41,75	3	39	42,75
Image mean	2	22	44,68	3	43	42,17	2	44	42,20			
Total mean	2	36	43,12									

Table 4.1: Subjective calibration results for sensor ViPA-1

Person	Image 1			Image 2			Image 3			Person mean		
	ESV	TV	Size	ESV	TV	Size	ESV	TV	Size	ESV	TV	Size
1	3	61	42,19	3	73	41,07	2	54	42,87	3	63	41,99
2	3	50	43,20	4	73	41,14	0	30	45,03	2	51	43,24
3	3	61	42,19	3	50	43,20	2	95	39,17	3	69	41,43
4	2	69	41,43	2	81	40,27	2	91	39,39	2	80	40,35
5	2	52	43,08	2	91	39,39	2	92	39,29	2	78	40,52
6	2	68	41,46	2	60	42,35	2	52	43,08	2	60	42,35
7	2	71	41,14	1	69	41,36	2	95	39,17	2	78	40,52
8	3	89	39,74	2	73	40,96	2	62	42,17	2	75	40,82
9	3	84	40,08	3	73	41,07	2	91	39,39	3	83	40,2
Image mean	3	67	41,65	2	71	41,14	2	74	40,90			
Total mean	2	71	41,14									

Table 4.2: Subjective calibration results for sensor ViPA-2

tensive procedure should be implemented.

It was observed that the values of ESV and TV significantly influence both number of detected particles and corresponding particle size. Therefore, for both microscopes applied in the system, different experiments were performed for following set of values of selectable parameters:

- ESV: {0, 1, 2, ..., 10}
- TV: {30, 31, 32, ..., 90}

This resulted in around 620 experiments performed on each of the sensors. Each

experiment was conducted under the same steady flow rate. For all experiments, information about the number of particles and their sizes was stored in separate files. It was decided to find the optimal set of selectable calibration parameters by comparison of empirical distributions of detected particles with the true distribution information provided by BS-Partikel. As relatively high number of experiments was conducted on both of microscopic sensors, quantitative comparison of distributions was performed instead of graphical inspections of histograms.

4.2.1 Z-test and Number of Particles

The mean μ_{BS} and standard deviation σ_{BS} values provided by BS-Partikel were considered as known population parameters of particle size. It should be mentioned that filtering was performed at the beginning of the procedure in order to remove outliers $5\sigma_{BS}$ away from μ_{BS} in datasets from all experiments. Mean $\hat{\mu}$ and standard deviation $\hat{\sigma}$ values obtained from each of the experiments were considered as sample parameters. In order to see whether the data from a sample comes from the BS-Partikel population, z-tests were conducted for all experiments. Therefore, the following null hypothesis H_0 and alternative hypothesis H_1 were formulated and presented accordingly in Equations 4.1 and 4.2.

$$H_0 : \mu = \mu_{BS} \quad (4.1)$$

$$H_1 : \mu \neq \mu_{BS} \quad (4.2)$$

If for some experiments, null hypothesis is accepted, it can be stated that the data coming from this experiment comes from the BS-Partikel distribution. The alternative hypothesis states otherwise. In order to decide about acceptance or rejection of a null hypothesis, test statistics were calculated for all experiments, described in Equation 4.3 [21].

$$z = \frac{\hat{\mu} - \mu_{BS}}{\sigma_{BS} / \sqrt{n}} \quad (4.3)$$

Number of detected particles n influences the calculated test statistic. Performed tests were two-sided and a default 95% confidence level was selected. This contributes to the critical value of z-score equal to $\pm 1,96$. Therefore, if for some experiment the absolute value of z is greater than 1,96, the null hypothesis is rejected and the alternative hypothesis is accepted.

It can be observed in Equation 4.3 that it is harder to accept the null hypothesis, when the sensor detected greater number of particles n . Therefore, in order to eliminate experiments with passed z-test and small n , only experiments with $n > 1000$ were considered as potential candidates of optimal sensor settings. All experiments which

passed z-test and requirement of 1000 detected particles are represented as blue rectangles in heatmaps depicted in Figure 4.4 for sensor ViPA-1 and in Figure 4.5 for sensor ViPA-2.

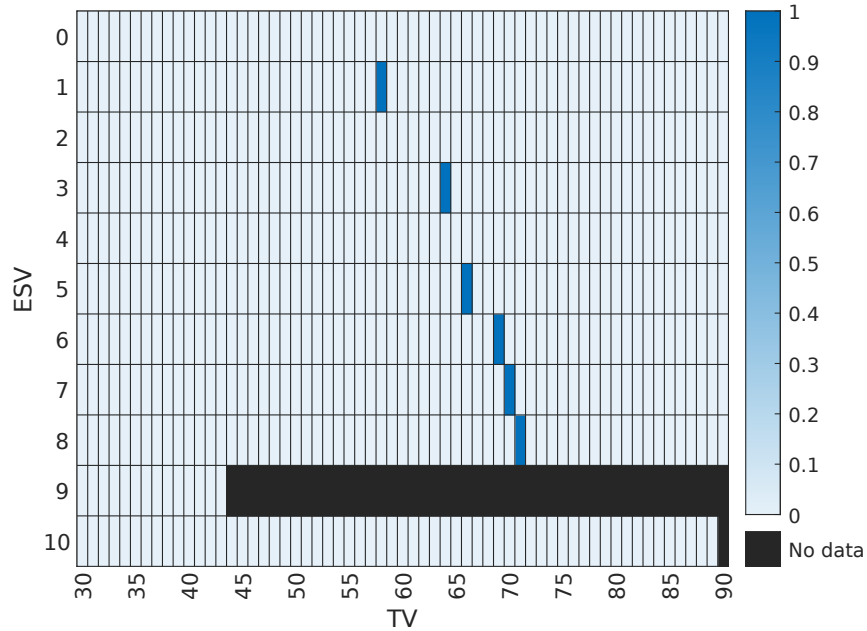


Figure 4.4: Experiments with passed z-test and $n > 1000$ for sensor ViPA-1

For experiments with white field box, null hypothesis was rejected, and for experiments with black field box data was not captured due to a technical issue. Although for each of the sensors, 6 experiments passed aforementioned requirements, different values of ESV and TV were observed in these experiments. This observation indicates that optimal settings of calibration parameters may be different even in the same system or application.

It is desired to find the optimal set of calibration parameters not only in terms of proximity of sample mean $\hat{\mu}$ to population μ_{BS} , but also in terms of general proximity between desired and empirical distributions. During z-test, the difference in variance between sample and population is not investigated. Thus, some experiments which passed the aforementioned requirements may have a standard deviation significantly different from the population standard deviation σ_{BS} . In order to overcome the problem of different variance, several methods were used, which are further described below in Subsections 4.2.2, 4.2.3, 4.2.4, 4.2.5 and 4.2.6.

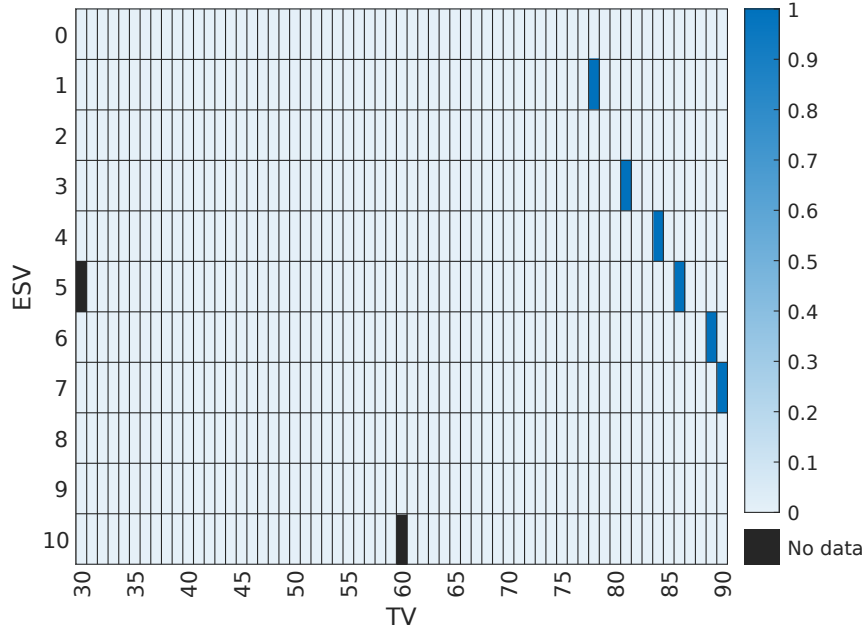


Figure 4.5: Experiments with passed z-test and $n > 1000$ for sensor ViPA-2

4.2.2 Kolmogorov-Smirnov Test

Kolmogorov-Smirnov Test (KS-test) is a statistical test based on measuring proximity between empirical cumulative distribution function (CDF) and hypothesised cumulative distribution function [22]. In the analysed case, the empirical CDFs were obtained through collected data from each of the experiments, however BS-Partikel parameters μ_{BS} and σ_{BS} were treated as parameters of the hypothesised CDF. In the KS-test, the null hypothesis states that empirical CDF is equal to hypothesised CDF. The alternative hypothesis states otherwise. To accept or reject the null hypothesis, the test statistic d_{KS} is calculated using the formula described in Equation 4.4.

$$d_{KS} = \max_x (|\hat{F}(x) - F_{BS}(x)|) \quad (4.4)$$

d_{KS} may be defined as a maximum absolute difference between the empirical CDF $\hat{F}(x)$ and the hypothesised CDF $F_{BS}(x)$, where x is a particle size. The null hypothesis is rejected when d_{KS} value is greater than the critical value, equal to $1.36/\sqrt{n}$. Due to dependency of critical value to number of detected particles n , KS-test was passed only in few experiments with relatively small n . Moreover, none of the potential candidates presented in Figures 4.4 and 4.5 passed KS-test. Despite rejection of the null hypothesis in all potential candidates, for all of them the test statistic d_{KS} was calculated and treated as an absolute measure of goodness-of-fit.

All experiments which passed the z-test and the requirement of $n > 1000$ were sorted in the ascending order with respect to d_{KS} in Table 4.3. Experiments with the lowest d_{KS} values were considered as the ones with the best sets of calibration settings according to the KS-test.

(a) ViPA-1			(b) ViPA-2		
ESV	TV	d_{KS}	ESV	TV	d_{KS}
3	64	0,1302	4	84	0,1125
1	58	0,1460	5	86	0,1171
5	66	0,1639	3	81	0,1449
6	69	0,1854	6	89	0,1525
7	70	0,2256	7	90	0,1776
8	71	0,2357	1	78	0,1890

Table 4.3: Best performing experiments according to d_{KS}

4.2.3 Chi-square Test

Chi-square test is another statistic test, which can be used for measuring proximity of a sample and a distribution. It is a variance test, thus it utilizes only the information about the difference in standard deviation. For analysed application, null hypothesis H_0 , described by Equation 4.5, states that the sample data of an experiment with a standard deviation s comes from a normal distribution with a hypothesised standard deviation σ_{BS} . The alternative hypothesis H_1 , described by Equation 4.6, states otherwise [23].

$$H_0 : s = \sigma_{BS} \quad (4.5)$$

$$H_1 : s \neq \sigma_{BS} \quad (4.6)$$

In order to accept or reject the null hypothesis H_0 , for all experiments a test statistic T was calculated. If the test statistic T exceeds critical value T_{crit} , the null hypothesis is rejected.

$$T = (n - 1) \frac{s^2}{\sigma_{BS}^2} \quad (4.7)$$

It can be observed in Equation 4.7 that a test statistic T depends on the sample size n . Similarly to KS-test, significant amount of Chi-square tests were rejected, as large n impedes acceptance of null hypothesis. Therefore, a new metric T_{norm} was proposed. As observed in Equation 4.8, T_{norm} is denormalized, and converted in a way that the best-case scenario occurs when it equals 0. The larger the difference between s and σ_{BS} occurs for an experiment, the larger T_{norm} is obtained.

$$T_{norm} = \left| 1 - \frac{T}{n-1} \right| = \left| 1 - \frac{s^2}{\sigma_{BS}^2} \right| \quad (4.8)$$

All experiments which passed the z-test and the requirement of $n > 1000$ were sorted in the ascending order with respect to T_{norm} in Table 4.4. Experiments with the lowest T_{norm} values were considered as the ones with the best sets of calibration settings according to the Chi-square test.

(a) ViPA-1			(b) ViPA-2		
ESV	TV	T_{norm}	ESV	TV	T_{norm}
3	64	0,4040	4	84	0,0544
5	66	0,5542	5	86	0,3063
6	69	0,6622	6	89	0,4020
7	70	0,7744	3	81	0,4063
8	71	0,7871	7	90	0,5091
1	58	0,9770	1	78	1,0298

Table 4.4: Best performing experiments according to T_{norm}

4.2.4 KL Divergence

Instead of being a statistical test like the aforementioned KS test or Chi-square test, Kullback-Leibler (KL) divergence, or relative entropy, is a measure of statistical distance between 2 populations and is described by Equation 4.9 [24]. KL divergence $D_{KL}(P||Q)$ may be interpreted as an expected surprise or logarithmic difference between a probability distribution $Q(x)$ considered as a model and a true probability distribution $P(x)$ [25].

$$D_{KL}(P||Q) = \sum_x P(x) \log\left(\frac{P(x)}{Q(x)}\right) \quad (4.9)$$

In order to acquire these probability distributions for each of the experiments, detected particle data was grouped into bins with a fixed width. The individual probability of a bin was calculated as a ratio of detected particles in a bin to total number of particles detected in this experiment. These individual bin probabilities values were assigned to the middle particle size in a bin, and thus a probability distribution $P(x)$ was obtained. Using the same set of middle particle sizes of bins and BS-Partikel parameters μ_{BS} and σ_{BS} , probability distribution $Q(x)$ was obtained. In Figure 4.6, the binning procedure and aforementioned evaluation of probability distributions is depicted on the part of a histogram of one of the experiments.

The value of a probability of a single bin depends on its width, thus $D_{KL}(P||Q)$ is influenced by bin width as well. However, one of the requirements of KL divergence is

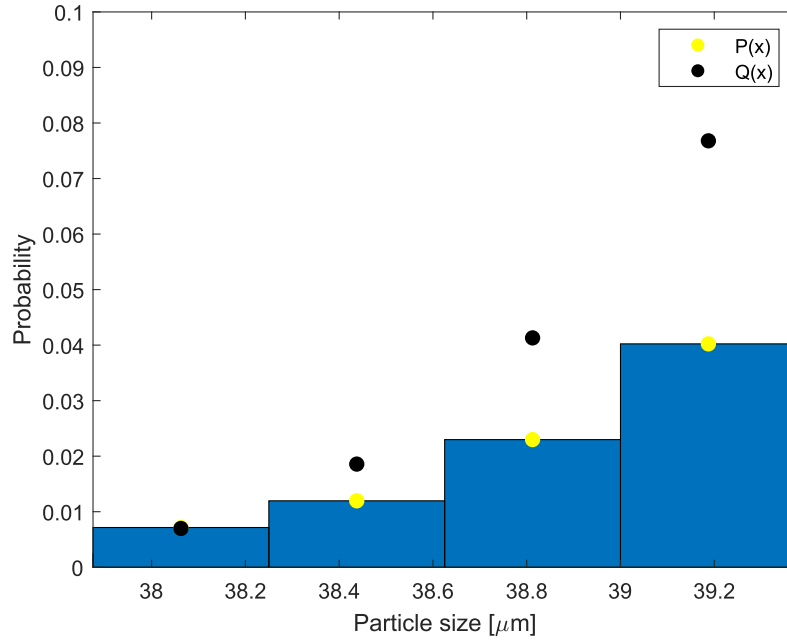


Figure 4.6: Visualisation of binning, $P(x)$ and $Q(x)$

the absolute continuity of $P(x)$ and $Q(x)$. If the bin is too narrow, there might be a bin without any detected particles in a specific range, thus for this bin $P(x) = 0$ and the KL divergence may not be computed. Therefore, it was decided to set the bin width for all experiments to the length of a pixel on the picture, which equals $0,375 \mu\text{m}$.

As the $D_{KL}(P||Q)$ aims to measure a distance between $P(x)$ and $Q(x)$ the larger it is, the more distributions differ from each other. Therefore, all experiments which passed the z-test and the requirement of $n > 1000$ were sorted in the ascending order with respect to $D_{KL}(P||Q)$ in Table 4.5. For some experiments, despite quite large bin width, KL divergence could not be calculated due to at least one empty bin. Experiments with the lowest $D_{KL}(P||Q)$ values were considered as the ones with the best sets of calibration settings according to the KL divergence.

4.2.5 JS Divergence

Although KL divergence may measure distance between 2 distributions, it is not a symmetrical divergence as $D_{KL}(P||Q) \neq D_{KL}(Q||P)$. It was observed that the order of experiments in Table 4.5 would be different if experiments were sorted in ascending order according to $D_{KL}(Q||P)$. Therefore, Jensen-Shannon (JS) divergence was calculated for all experiments, which is a symmetrical version of KS divergence. It is defined by Equations 4.10 and 4.11 [26].

(a) ViPA-1			(b) ViPA-2		
ESV	TV	$D_{KL}(P Q)$	ESV	TV	$D_{KL}(P Q)$
3	64	0,1582	4	84	0,1551
5	66	0,2618	5	86	0,1843
1	58	0,3194	3	81	0,2125
6	69	-	6	89	0,2231
7	70	-	1	78	0,3856
8	71	-	7	90	-

Table 4.5: Best performing experiments according to $D_{KL}(P||Q)$

$$JSD(P||Q) = \frac{1}{2}D_{KL}(P||M) + \frac{1}{2}D_{KL}(Q||M) \quad (4.10)$$

$$M = \frac{1}{2}(P + Q) \quad (4.11)$$

All experiments which passed the z-test and the requirement of $n > 1000$ were sorted in the ascending order with respect to $JSD(P||Q)$ in Table 4.6. Similarly, as for KL divergence, for some experiments JS divergence could not be calculated due to at least one empty bin. Experiments with the lowest $JSD(P||Q)$ values were considered as the ones with the best sets of calibration settings according to the JS divergence.

(a) ViPA-1			(b) ViPA-2		
ESV	TV	$JSD(P Q)$	ESV	TV	$JSD(P Q)$
3	64	0,0420	4	84	0,0356
1	58	0,0439	3	81	0,0419
5	66	0,0706	5	86	0,0443
6	69	-	6	89	0,0568
7	70	-	1	78	0,0574
8	71	-	7	90	-

Table 4.6: Best performing experiments according to $JSD(P||Q)$

4.2.6 Sum of Squared Errors

Despite solving the issue of symmetry, JS divergence is susceptible to empty bins, thus for some experiments could not be computed. Therefore, Sum of Squared Errors (SSE) between probability distributions $P(x)$ and $Q(x)$ was calculated for all experiments based on the same bins as for KL and JS divergences. SSE is defined by Equation 4.12.

$$SSE = \sum_x (P(x) - Q(x))^2 \quad (4.12)$$

The lower the value of SSE is for an experiment, the more close to each other are $P(x)$ and $Q(x)$. There is no requirement of absolute continuity for this measure of goodness-of-fit. All experiments which passed the z-test and the requirement of $n > 1000$ were sorted in the ascending order with respect to SSE in Table 4.7. Experiments with the lowest SSE values were considered as the ones with the best sets of calibration settings according to the sum of squared errors.

(a) ViPA-1			(b) ViPA-2		
ESV	TV	SSE	ESV	TV	SSE
1	58	0,0208	4	84	0,0226
3	64	0,0297	3	81	0,0246
5	66	0,0478	5	86	0,0293
6	69	0,0687	6	89	0,0325
7	70	0,1037	1	78	0,0327
8	71	0,1210	7	90	0,0528

Table 4.7: Best performing experiments according to SSE

4.2.7 Comparison of Methods

On all tests, which fulfil preliminary condition of passed z-test and requirement of $n > 1000$, various aforementioned methods were applied. According to these tests and measures, out of Tables 4.3, 4.4, 4.5, 4.6 and 4.7 the best sets of calibration settings were presented in Table 4.8.

(a) ViPA-1				(b) ViPA-2			
Method	ESV	TV	Skewness	Method	ESV	TV	Skewness
KS-test	3	64	-0,7046	KS-test	4	84	-0,7356
Chi-test	3	64	-0,7046	Chi-test	4	84	-0,7356
KL divergence	3	64	-0,7046	KL divergence	4	84	-0,7356
JS divergence	3	64	-0,7046	JS divergence	4	84	-0,7356
SSE	1	58	-1,1373	SSE	4	84	-0,7356

Table 4.8: Comparison of the best calibration settings from different methods

For sensor ViPA-2, all applied methods suggested using ESV of 4 and TV of 84. However, for sensor ViPA-1, 4 methods suggested using ESV of 3 and TV of 64, while SSE

proposed ESV of 1 and TV of 58 as the best set of calibration settings. In order to choose between these 2 candidates, additionally skewness was calculated for all experiments, based on Equation 4.13, where x_i is i th detected particle in an experiment. Skewness is a measure of asymmetry. A probability distribution can be left skewed if its skewness is negative, and right skewed if it is positive. A perfectly symmetric distribution has skewness equal to 0 [27].

$$skewness = \frac{\sqrt{n(n-1)}}{n-2} \frac{\frac{1}{n} \sum_{i=1}^n (x_i - \hat{\mu})^3}{\sqrt{\frac{1}{n} \sum_{i=1}^n (x_i - \hat{\mu})^2}} \quad (4.13)$$

It can be observed in Table 4.8, that a distribution with calibration parameters suggested for sensor ViPA-1 by SSE is less symmetrical. Therefore, for this sensor, ESV of 3 and TV of 64 were considered as the optimal set of calibration parameters. As for sensor ViPA-2 all methods suggested the same set of parameters, ESV of 4 and TV of 84 was considered as an optimal set of calibration parameters. Probability histograms of particle data from experiments with aforementioned best sets of calibration parameters are presented in Figures 4.7 and 4.8 for sensors ViPA-1 and ViPA-2 respectively. The red plot represents the theoretical normal probability distribution based on BS-Partikel parameters μ_{BS} and σ_{BS} .

It can be observed in Figures 4.7 and 4.8, that probabilities of bins follow the desired probability shape. These graphical solutions confirm conclusions from quantitative measures and tests.

4.3 Validation Procedure

Although the optimal set of calibration parameters could correctly detect particles described by parameters μ_{BS} and σ_{BS} , it is necessary to ensure that sensors may reliably detect particles with different size. Therefore, larger particles from the same manufacturer were added to the system with mean μ_{valBS} of 79,4 μm and standard deviation σ_{valBS} of 1,75 μm . The PDF and CDF of larger particles can be observed in Figure 3.6.

Probability histograms of validation particles, detected via optimal sets of calibration parameters, are presented in Figures 4.9 and 4.10 for sensors ViPA-1 and ViPA-2 respectively. Additionally, the probability distribution based on μ_{valBS} and σ_{valBS} was plotted. Particles depicted in Figures 4.9 and 4.10 come from a range of 5 σ_{valBS} away from μ_{BS} . The same bin width was applied in order to create validation histograms.

It can be observed that detected particles follow the shape of probability distribution based on μ_{valBS} and σ_{valBS} . In order to further validate detected particles with larger size, z-tests were conducted for both sensors. Similarly to the procedure described in Subsection 4.2.1, sample mean $\hat{\mu}_{val}$ was obtained based on particles 5 σ_{valBS} away from μ_{valBS} . Moreover, in this interval, using optimal calibration settings, 738 particles were detected for ViPA-1 and 823 for ViPA-2. Based on number of detected particles

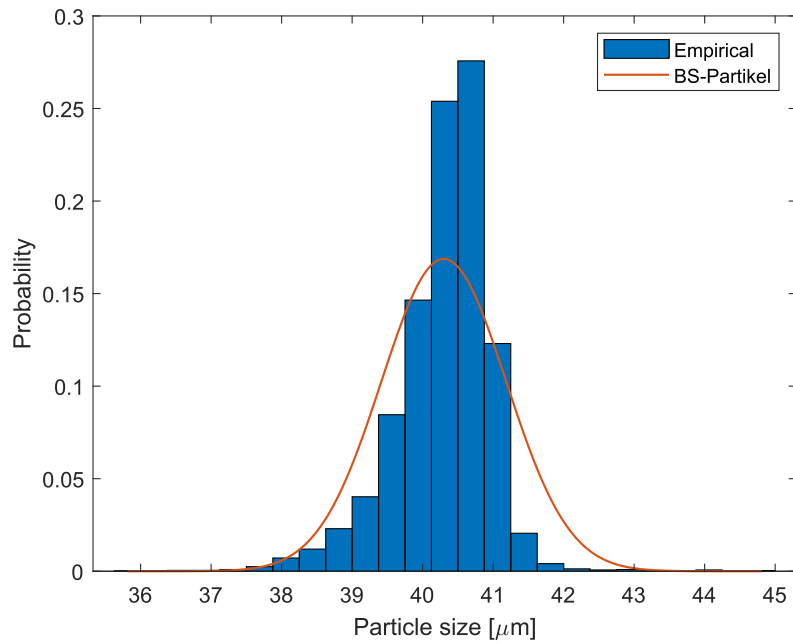


Figure 4.7: Probabilities for ViPA-1, ESV: 3, TV: 64

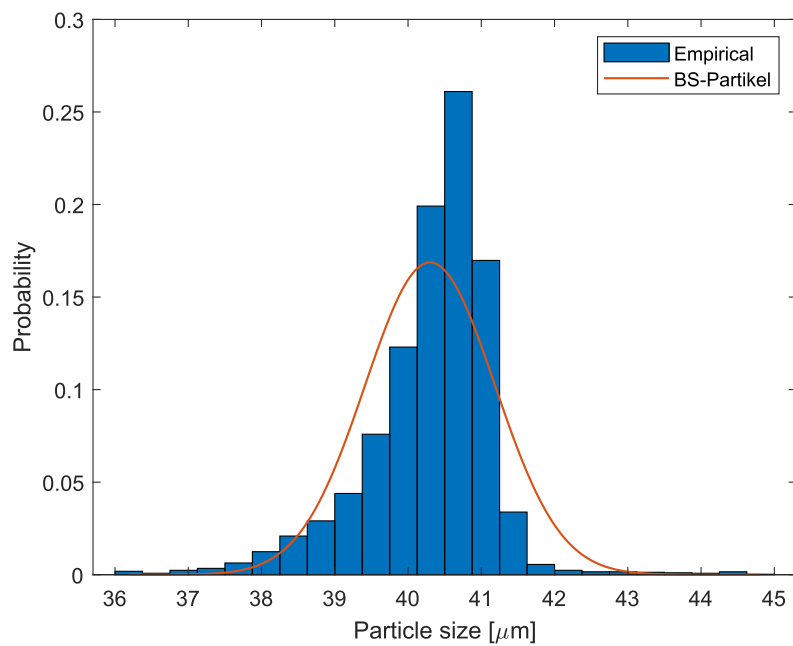


Figure 4.8: Probabilities for ViPA-2, ESV: 4, TV: 84

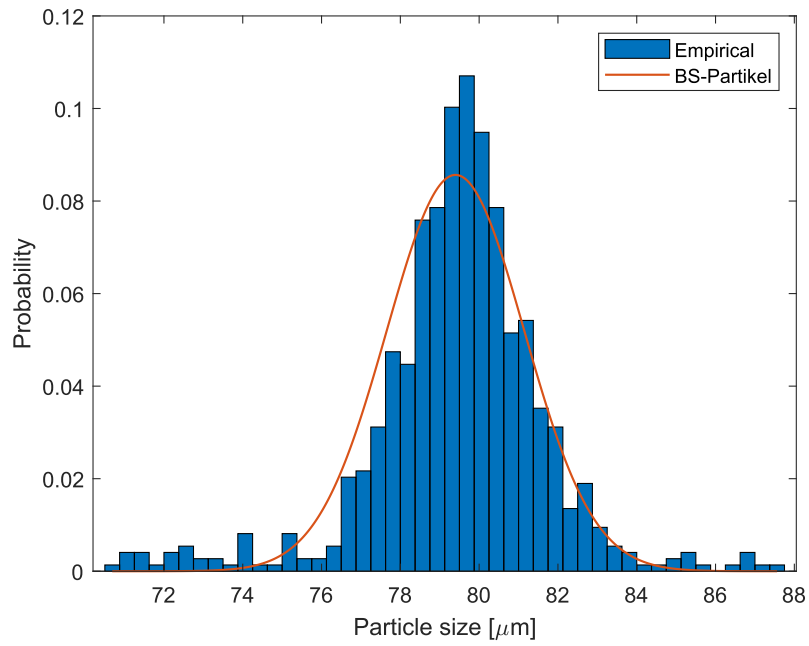


Figure 4.9: Validation probabilities for ViPA-1, ESV: 3, TV: 64

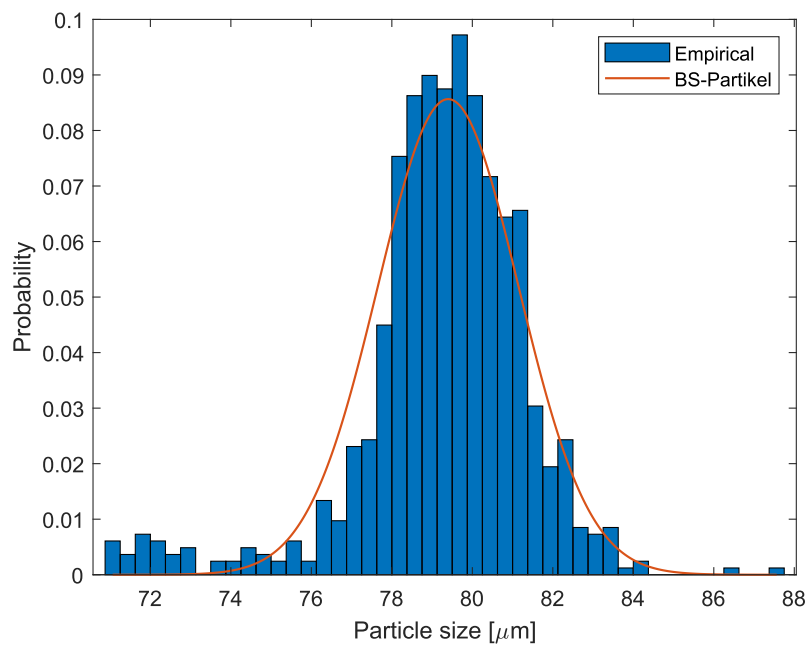


Figure 4.10: Validation probabilities for ViPA-2, ESV: 4, TV: 84

and sample mean $\hat{\mu}_{val}$, z-test statistic was calculated using the formula, described in Equation 4.3. The absolute value of z equals 1.09 for ViPA-1 and 2 for ViPA-2, which for both of these sensors is smaller than the critical value of 2,58 for 99% confidence level. Therefore, null hypothesis was accepted for both sensors and this further validates detection performance of sensors for larger particles.

Although in calibration and validation procedures the performance of particle detection was analysed in the proximity of μ_{BS} and μ_{valBS} , it is worth mentioning if and how many particles with some other size were detected in the system. Ideally, there should be very few particles detected outside analysed intervals. However, it can be observed in Figures 4.11 and 4.12, that there are some particles detected, which have smaller size than μ_{BS} . Especially, the undesired peak occurs for the smallest detected size of particles. This may indicate that some miniature particles were detected along the edge of a significantly bigger particle. Moreover, there might be some additional debris in the water apart from BS-Partikel particles, such as dirt. It may seem that such peak might influence calculation of microplastic concentration. However, the contribution of volume of the smallest particles should be insignificant, as the volume of a detected particle is proportional to the cube of its size. Therefore, obtained distribution of detected particles in Figures 4.11 and 4.12 may be considered as satisfactory.

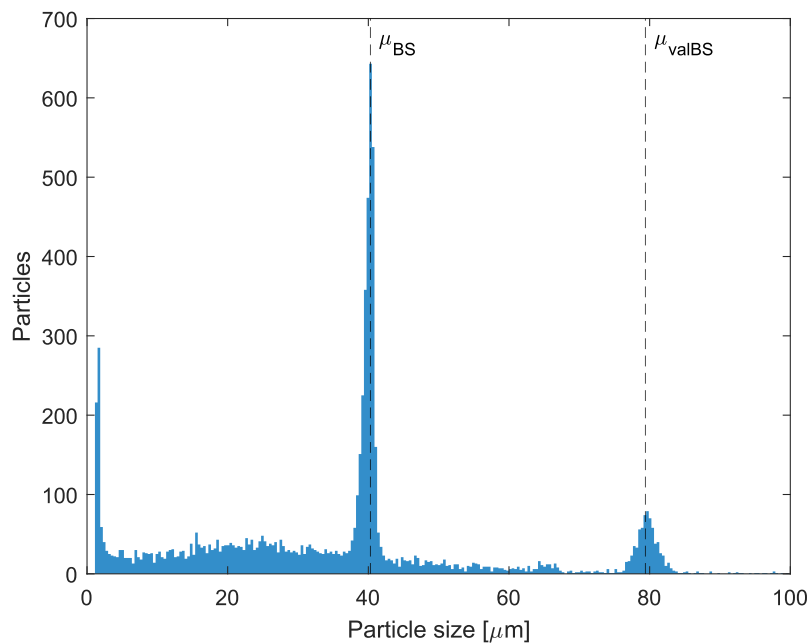


Figure 4.11: Histogram of all detected particles for ViPA-1, ESV: 3, TV: 64

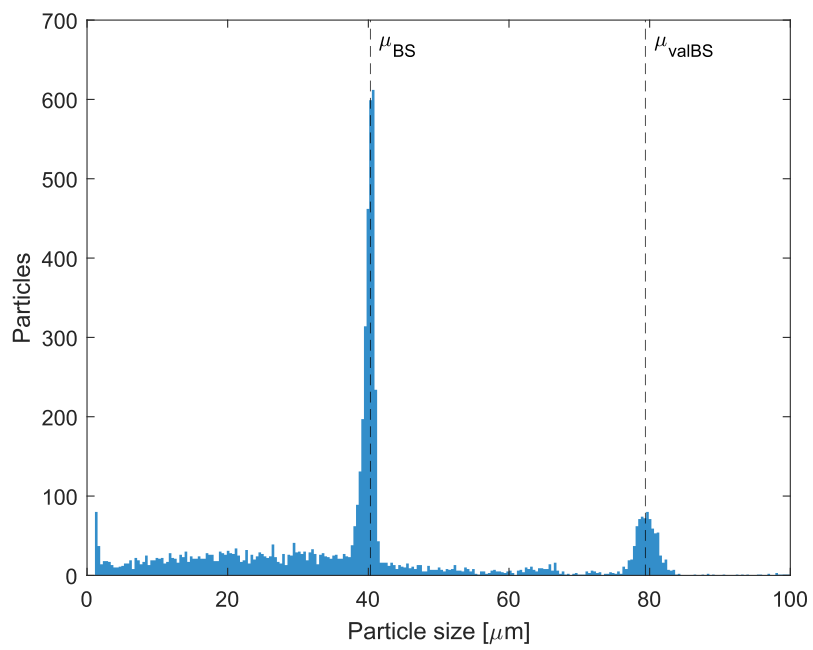


Figure 4.12: Histogram of all detected particles for ViPA-2, ESV: 4, TV: 84

Chapter 5

Assessment of Hydrocyclone Separation Capability

In this chapter, the description of the experiment design will be provided. Data pre-processing procedure will be explained as well, along with the analysis of hydrocyclone separation efficiency.

5.1 Experiment Design

For the main experiment, the setup described in Section 3.2.2 was used. The main objective of the experiment is to analyse the performance of hydrocyclone under different operating condition. Underflow V_u and overflow V_o valve opening angles determine the split between two flow streams. Therefore, it was decided to treat these signals as manipulated variables, defining the experiment design.

The grid of values was designed for manipulated variables. If valve angle equals 0, the valve is fully closed, whereas if valve angle equals 1, the valve is fully open. It was decided that throughout the experiment V_u would increase from 0.5 to 1, with a step of 0.05. For each underflow valve angle V_u opening, the overflow valve angle V_o would increase from 0 to 0.5, also with a step of 0.05. Thus, the experiment was divided into 121 segments with constant V_o and V_u . The duration of the particular segment was 5 minutes, therefore the whole experiment took around 10 hours and 10 minutes. The change of V_o and V_u over time is presented in Figure 5.1, along with other fundamental signals from the setup.

All the sensors depicted in Figure 3.7 were performing measurements simultaneously, with the same sampling rate of 0.01 s. All remaining valves of the setup were controlled in a manner to maintain constant inlet sidestream Q_{is} and underflow sidestream Q_{us} flow rates throughout the experiment, which is visible in Figure 5.1. This enabled appropriate monitoring conditions for ViPA sensors. Due to the increase of V_u throughout the experiment, and the constant maximum power of the centrifugal pump, inlet Q_i

and underflow Q_u flow rates were increasing with time, which is also evident in Figure 5.1.

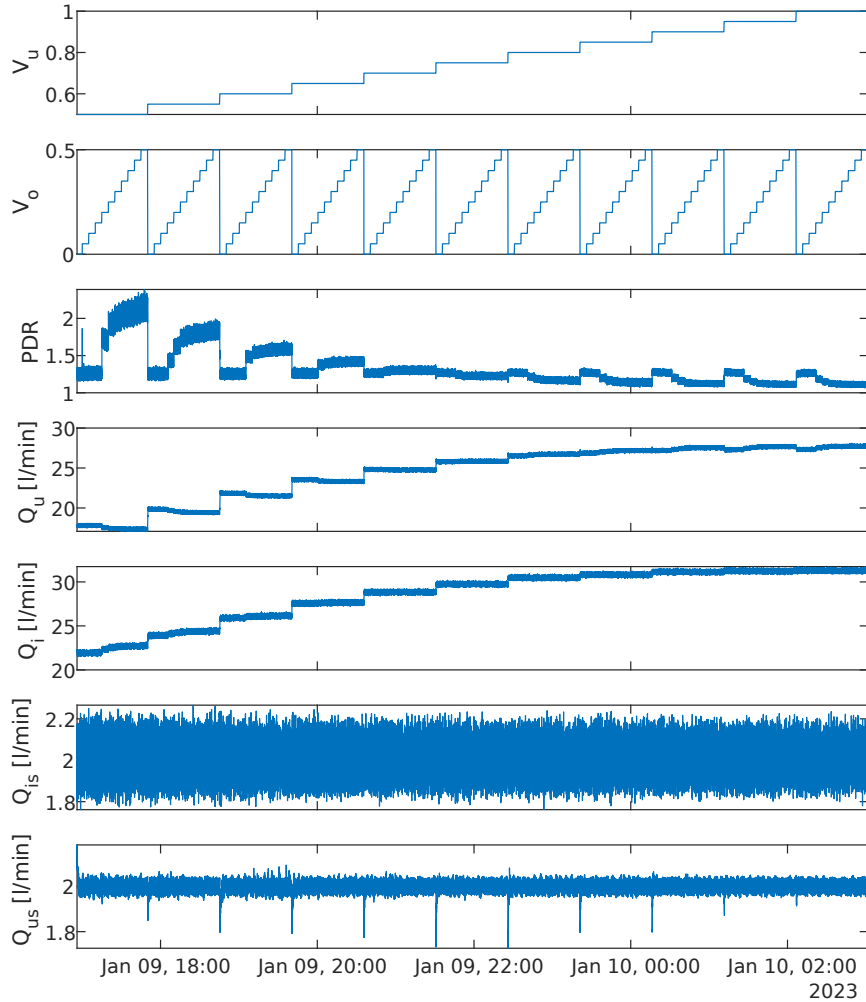


Figure 5.1: Operating conditions during the experiment

Based on inlet P_i , underflow P_u , and overflow P_o pressure measurements, Pressure Difference Ratio (PDR) was calculated with respect to Equation 5.1. PDR can be considered as a close linear approximation of a flow split, defined as Q_o/Q_i [17]. Therefore, it is an important parameter, which may be used for the control purpose of a hydrocyclone to ensure its adequate separation efficiency. The obtained PDR throughout the duration of experiment was presented as well in Figure 5.1.

$$PDR = \frac{P_i - P_o}{P_i - P_u} \quad (5.1)$$

Measurements of all other signals from the setup are depicted in Appendix A, in Figures A.1, A.2 and A.3. It should be noted that the experiment was conducted by Dennis Severin Hansen and Stefan Jespersen on the 9th of January 2023, prior to the beginning of this project. However, all data analysis was performed by the author of this thesis.

5.2 Data Preprocessing

5.2.1 ViPA Data Preprocessing

During the experiment, ViPA sensors were not calibrated optimally with respect to ESV and TV. Instead, some initial calibration settings were selected arbitrarily. ViPA software saved information from both sensors in *.rvd* format files, which contain tabular data of detected particles throughout the experiment. Additionally, pictures of frames with at least 1 detected particle were saved in *.bmp* format. This enabled ViPA software to use these images from the original experiment along with the best calibration settings as inputs, to perform a new image processing procedure. Thus, new *.rvd* files were obtained for best calibration settings for both sensors.

Each row of a *.rvd* file contains information about numerous parameters of a detected particle. The key parameters of ViPA software were described above in Section 3.1. Additionally, the information about the frame number and timestamp of the detected particle is provided.

Contrary to *.rvd* files generated during the experiment, the timestamp in *.rvd* files with the best calibration settings refers to the date time of computation of an image through software. Therefore, it was necessary to link particles detected through the best calibration with particles detected through the initial calibration settings, via corresponding picture number. Before doing that, it was essential to accumulate size and concentration of particles on the same frame.

It was observed that for some small particles, around $2 \mu\text{m}$, *.bmp* pictures were not saved, despite being included in *.rvd* files for initial calibration settings. ViPA software was not able to use their pictures for generation of *.rvd* files for the best calibration settings, thus these particles were excluded from further analysis. Although 17% and 9% of data was discarded for sensors ViPA-1 and ViPA-2 respectively, these particles would not contribute significantly to calculation of concentration level due to their small size.

Timestamps of particles were recorded as Excel date numbers. These were converted to a meaningful date format, which was in accordance with the date of the experiment.

As mentioned above, *.rvd* files store information only about frames where at least 1 particle is detected. Therefore, timestamps of frames with no particles were not recorded. It is mandatory to have the information about number of empty frames, to calculate concentration and efficiency of the hydrocyclone during specific segment of the experiment. Thus, artificial empty frames were manually added to the dataset in between frames with detected particles, based on the frame number column. The size and the frame concentration were set to 0 in additional rows. Moreover, the timestamp was linearly interpolated for all new rows based on timestamps of neighbouring frames with detected particles. This procedure can be observed on the fragment of the dataset in Tables 5.1 and 5.2.

Picture	Frame	Size [μm]	Conc [Vppm]	Time from 1st particle [s]	...
3	50	3,4	3,2	0,8420	...
4	53	47,7	8634,7	0,9510	...

Table 5.1: Fragment of particle data before addition of empty frames

Picture	Frame	Size [μm]	Conc [Vppm]	Time from 1st particle [s]	...
3	50	3,4	3,2	0,8420	...
NaN	51	0	0	0,8783	...
NaN	52	0	0	0,9147	...
4	53	47,7	8634,7	0,9510	...

Table 5.2: Fragment of particle data after addition of empty frames

5.2.2 Signals Data Preprocessing

As mentioned in Section 5.1, other sensors from the setup were performing measurements simultaneously, thus there was no need for time alignment between these signals. Unfortunately, time of measurements was recorded only in seconds, thus there was no timestamp indicator defining the start or end of the experiment. It was decided to align the starting time of the sensors, hence the starting time of the experiment, with the timestamp of the first detected particle from sensor ViPA-1.

5.3 Efficiency Results

The aforementioned preprocessing of data from ViPA sensors was conducted on datasets from initial and best sets of calibration settings. Therefore, results for both scenarios of calibration are presented in this section.

Upon ensuring alignment of all signals with respect to time, it was possible to obtain specific values of concentration at a given set of manipulated variables V_u and V_o . The

concentration of a segment was obtained by computing the average of all individual frame concentrations during such segment. Concentrations of 0 from artificially added empty frames were included in the calculation of mean concentration value of a segment. Additional buffer was introduced in order to mitigate the aforementioned uncertainty associated with the exact starting time of the experiment. The buffer was set to 10%. This corresponds to discarding particles detected within the first 5% and last 5% of a segments' duration.

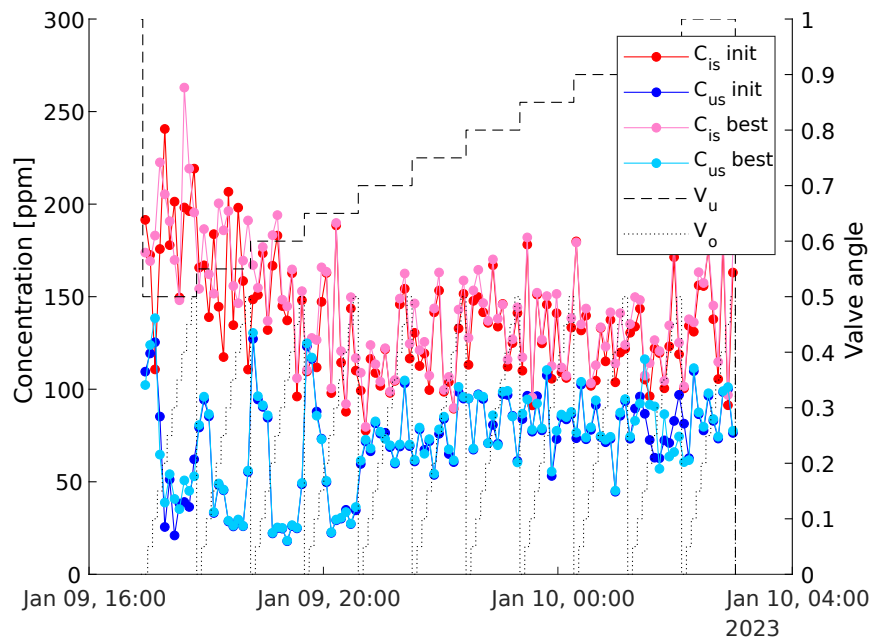


Figure 5.2: Concentration during the experiment for initial and best calibration settings

For both sensors, mean concentrations values were obtained for all segments. Figure 5.2 presents the dynamics of concentration throughout the experiment. In line with the diagram of the setup from Figure 3.7, ViPA-1 measured the inlet sidestream concentration C_{is} , whereas ViPA-2 measured the underflow sidestream concentration C_{us} . It can be observed that the inlet concentration decreased over time. This may be a consequence of microplastic adhesion to the surface of the tank throughout the experiment.

The separation efficiency of the hydrocyclone e was defined according to the formula in Equation 5.2. When the overflow side detected a low number of particles, the efficiency values were high, especially when the inlet stream was highly concentrated. It should be emphasised that ViPA sensors were detecting sidestream concentrations C_{is} and C_{us} , which were used as approximations of main stream concentrations C_i and C_u .

$$e = 1 - \frac{C_u}{C_i} \quad (5.2)$$

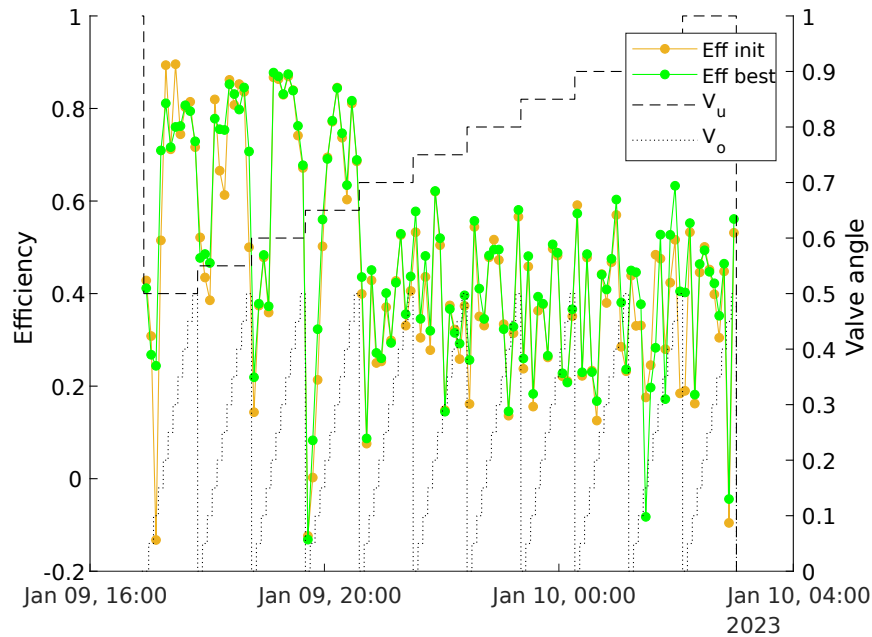


Figure 5.3: Efficiency during the experiment for initial and best calibration settings

Separation efficiency values e were calculated for every segment based on mean concentrations C_{is} and C_{us} . Figure 5.3 presents the change of e throughout the experiment. In order to simplify the analysis of e , its heatmaps for specific segments were depicted in Figures 5.4 and 5.5 for initial and best calibration settings.

It can be observed that the obtained efficiency values at specific segments do not vary significantly, despite using different ESV and TV. The highest efficiency, almost up to 90%, occurs in the region where V_o is at least 0.15, and V_u is no higher than 0.65. It may be stated that in this region, relatively less open V_u ensures that the inlet flow is not fast enough to disrupt the vortex core of lighter phase. Furthermore, V_o is sufficiently open, to allow for microplastic in the vortex to exit the hydrocyclone almost exclusively through the overflow outlet. Despite some local peaks of e in other regions, these other combinations of V_o and V_u fail to match the efficiency level in the aforementioned best region.

Efficiency e , defined by 5.2, focuses only on the underflow side, and does not take into account the amount of water exiting through the overflow side. It is an advantageous approach when the main objective is to ensure clarity of discharged water through underflow side. However, there might occur a case when observed e is satisfactory, but substantial amount of water exits the hydrocyclone through the overflow outlet with microplastics. This may happen when V_o is relatively high. One way to prevent this phenomenon is to slightly reduce the overflow valve angle.

Such potential situations may be observed in Figure 5.6, where the overflow flow

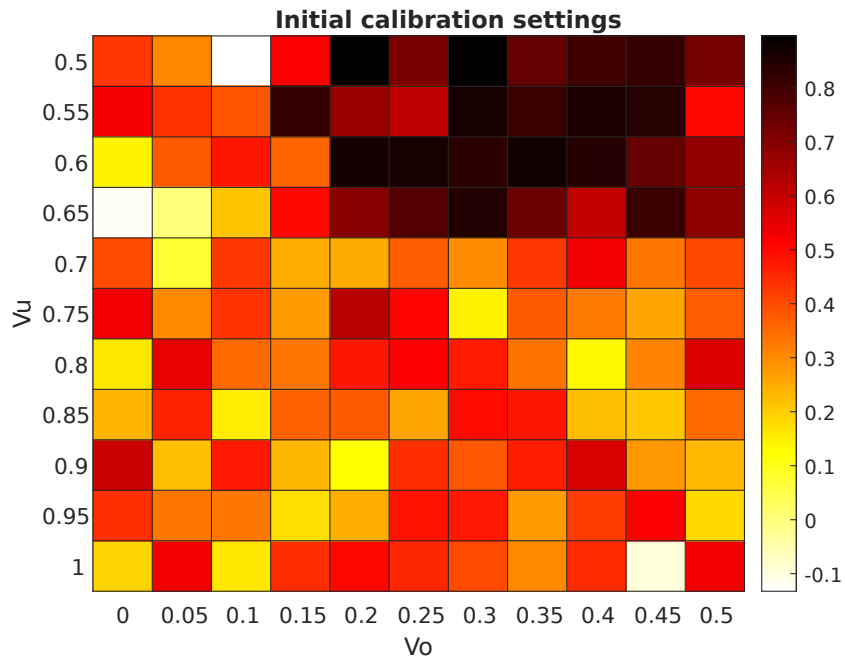


Figure 5.4: Separation efficiency heatmap for initial calibration settings

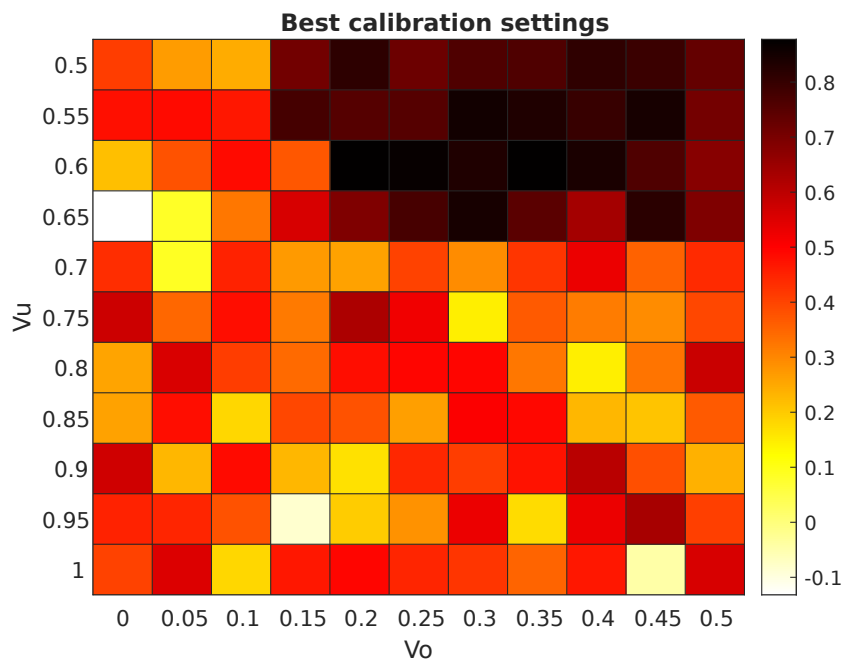


Figure 5.5: Separation efficiency heatmap for best calibration settings

rate Q_o was presented, with the efficiency under the best calibration settings. There was no sensor in the setup which was directly measuring Q_o , however this flow rate can be obtained based on information from other flow meters in the setup. Hence, Q_o was calculated using the formula in Equation 5.3. As the obtained signal carried a considerable amount of noise, the average values were calculated for specific segments of the experiment. These mean values were plotted in Figure 5.6.

$$Q_o = Q_i - Q_{is} - Q_u \quad (5.3)$$

It is evident that high efficiencies above 80% may be observed for different levels of Q_o . If it is desired to mitigate the issue of additional volume of water exiting through the overflow inlet, the level of Q_o , or its ratio to Q_i , could be a part of the selection algorithm of the optimal valve settings.

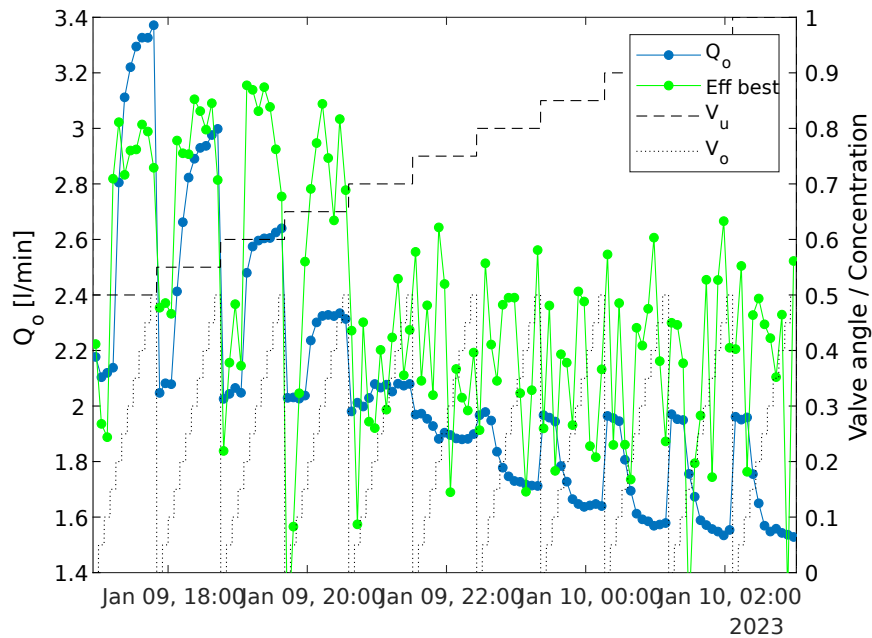


Figure 5.6: Efficiency and overflow flow rate Q_o

In Table 5.3, top 5 best performing settings of V_u and V_o according to the separation efficiency e are presented, for initial and best calibration settings respectively. Additionally, information considering Q_o was displayed as well. Different calibration settings proposed similar sets of openings of valves. Moreover, the difference between obtained efficiencies are insignificant. Therefore, it can be beneficial to select out of these top performers, the setting which has relatively low Q_o .

((a)) Initial ESV and TV				((b)) Best ESV and TV			
V_o	V_u	e	mean Q_o [l/min]	V_o	V_u	e	mean Q_o [l/min]
0,3	0,5	0,8958	3,22	0,2	0,6	0,8776	2,48
0,2	0,5	0,8937	2,81	0,35	0,6	0,8742	2,60
0,35	0,6	0,8695	2,60	0,25	0,6	0,8694	2,57
0,2	0,6	0,8674	2,48	0,3	0,55	0,8524	2,89
0,25	0,6	0,8635	2,57	0,45	0,55	0,8453	2,98

Table 5.3: Best performing valve settings according to e

5.3.1 Influence of Q_i and PDR

Apart from above analysed valve settings, there are other criteria which can define the performance of hydrocyclone.

Inlet flow Q_i determines the amount of energy entering the hydrocyclone. The flow of mixture needs to be high enough to create centripetal forces inside the hydrocyclone. With increase of Q_i , efficiency of separation also increases, until it reaches plateau. However, if Q_i is further increased, it reaches a certain maximum value, after which the separation is disturbed, due to the breakdown of particles or lack of sufficient pressure difference to allow for the core of particles to exit through the overflow outlet [17].

As mentioned in section 5.1, PDR can be considered as a close linear approximation of the flow split. If this split is too low, few particles may exit the hydrocyclone through the overflow side, as the overflow valve opening is too narrow. Increase of PDR results in higher efficiency. It is crucial to remember, that if V_o or PDR is too high, more water will exit the hydrocyclone through the overflow outlet.

Based on the above, both Q_i and PDR need to be maintained at specific level to ensure appropriate separation inside the hydrocyclone. These parameters are important variables of control strategies of hydrocyclones. Therefore, average values of Q_i and PDR were obtained for specific segments of the experiment, in the same manner as for mean values of Q_o .

Efficiency as a function of these key parameters is presented in Figures 5.7 and 5.8 for initial and best calibration settings respectively. Additionally, the best performing valve settings according to e are depicted in squares.

The uniform grid of V_o and V_u does not contribute to the uniform or rectangular grid for Q_i and PDR . It may be observed that for this hydrocyclone, PDR needs to be greater than 1.4 to obtain higher level of efficiencies. However, PDR does not need to be very high, as according to best ESV and TV , the highest efficiency occurs when PDR equals around 1,5.

It is evident that even for low values of observed Q_i , relatively high level of efficiency may be obtained. For larger values of Q_i , above 30 l/min, PDR achieved values not larger than 1.2, and e was found to be low. It should be noted that points in this area, were

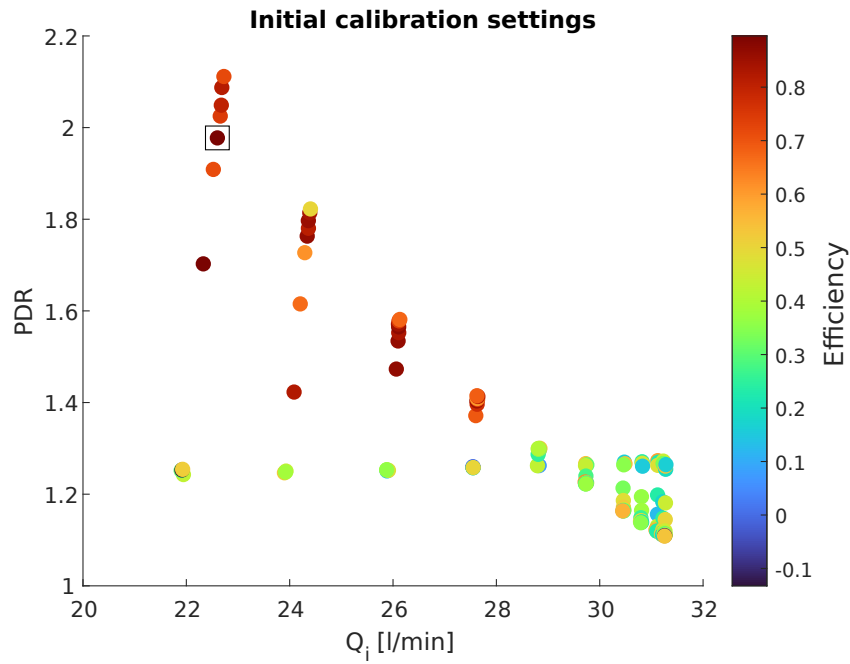


Figure 5.7: Efficiency vs Q_i and PDR for initial calibration settings

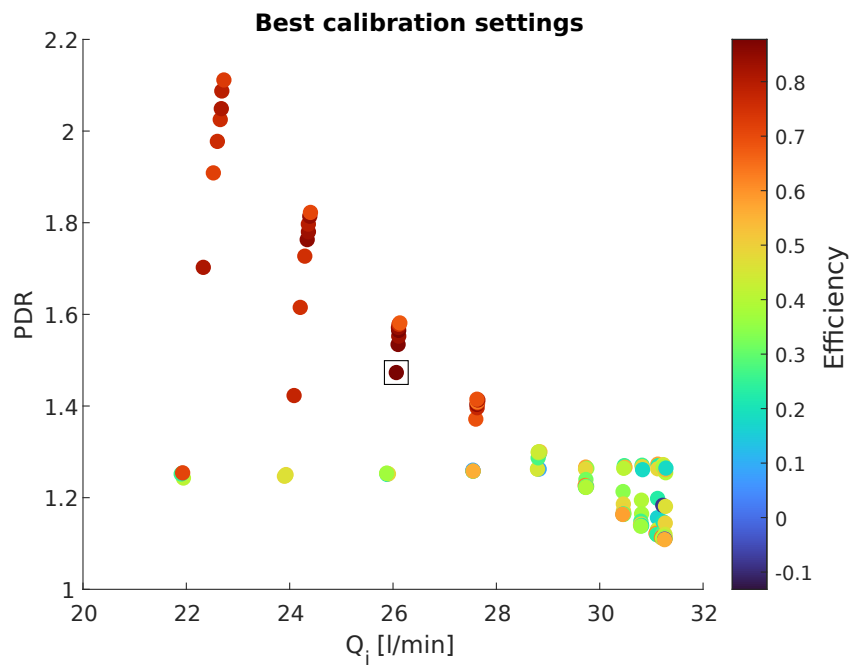


Figure 5.8: Efficiency vs Q_i and PDR for best calibration settings

collected in the second half of the experiment, with increasingly higher values of V_u . During this period, Q_o decreased and this can explain worse separation performance.

5.3.2 Size Distribution of Microbeads

It is interesting to observe not only the aforementioned overall efficiency of separation, but also how well were microbeads separated from water with respect to their size.

Therefore, ViPA data was preprocessed slightly differently from the procedure described in Section 5.2. Size of observed particles on the same frame was no longer accumulated. Instead, for each particle, individual parameters were saved. After further preprocessing, which included time alignment, it was evident during which segment of the experiment the particle was detected.

For segments with the highest e , size histograms of detected particles are presented in Figures 5.9 and 5.10, for initial and best calibration settings respectively. Additionally, size distributions of all particles observed throughout the whole duration of the experiment are presented in Appendix A, in Figures A.4 and A.5.

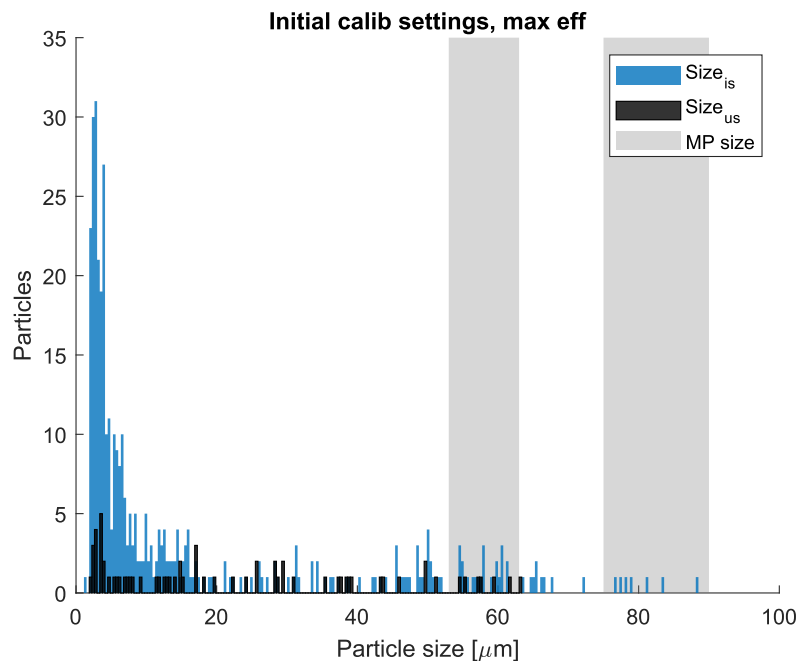


Figure 5.9: Histogram of detected particles for best efficiency and initial calibration settings

Particles detected on the inlet sidestream side are marked in blue, whereas particles detected on the underflow sidestream are marked in black. Gray regions indicate size range of added microbeads. As it was mentioned in Section 3.2.2, 4 bottles with smaller microbeads and 1 bottle with larger microbeads were added to the setup. This was

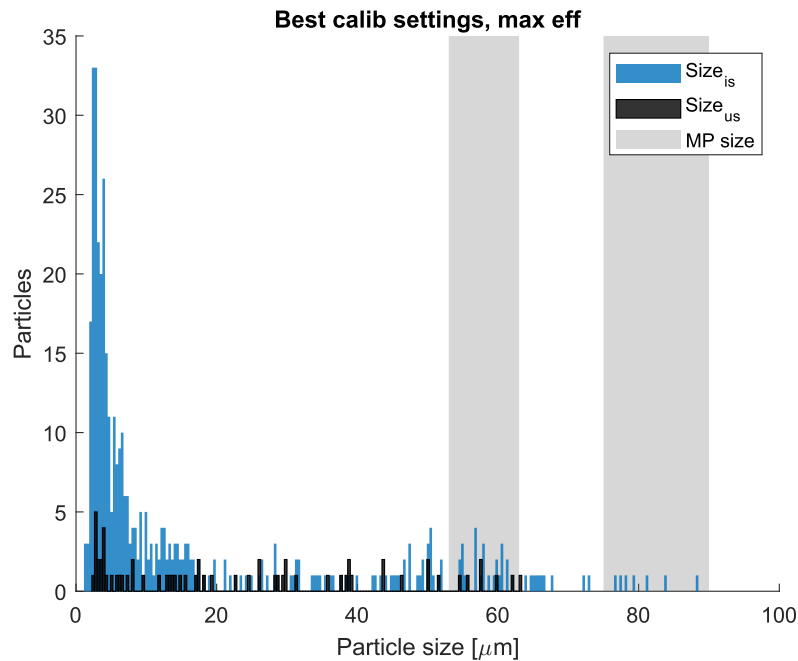


Figure 5.10: Histogram of detected particles for best efficiency and best calibration settings

confirmed by blue histograms, as more particles were detected in a range of 53 to 63 μm than in a range of 75 to 90 μm .

It can be observed in Figures 5.9 and 5.10, that none of the larger microbeads were spotted on underflow sidestream size. Furthermore, the majority of smaller microbeads were also not detected on underflow sidestream size. This phenomenon is in line with the separation principle of hydrocyclone, as it is easier to separate larger particles, due to their larger mass and inertia.

It is likely, that some larger microbeads could exit the hydrocyclone through the underflow outlet and later flowed with the main stream, so they are not evident in Figures 5.9 and 5.10. Nevertheless, based on information from available sensors, it can be stated that the hydrocyclone efficiently separated microbeads from water.

The majority of particles spotted on the underflow sidestream side were smaller than added microbeads. There is a possibility that some microbeads broke down into smaller pieces due to turbulence in the system. It could also be possible that these small particles are not microplastics, but some form of debris. Nevertheless, their contribution to the calculated concentration is insignificant, as the volume of such small particles is negligible, when compared with the volume of microbeads. It is worth mentioning that the significant majority of smaller particles seem to be separated from water.

Chapter 6

Conclusions

The task statement of this project asks whether hydrocyclone can be used for efficient separation of microplastics from water, and how its efficiency can be determined with a dynamic microscope. To answer this question, calibration of dynamic microscopes was performed. Data obtained from the experiment was preprocessed and the analysis of hydrocyclone performance was conducted with respect to its separation efficiency.

Based on the aforementioned procedure, the following conclusions may be drawn regarding the problem statement.

- By taking advantage of proposed statistical tests and measures, the optimal set of calibration settings is provided for ViPA sensors. This ensures appropriate measurement of size of particles, therefore more reliable information about separation efficiency may be obtained from dynamic microscopes.
- For specific settings of control valves, the region of efficiencies above 80% was found. According to optimally calibrated ViPA sensors, almost 88% of particles were separated from water. Hydrocyclones operating in other industries achieve similar separation efficiency. Therefore, it can be stated that hydrocyclone can be used for efficient separation of microplastics from water.
- Despite obtaining satisfactory levels of efficiency, some microplastic particles still remain in water. Considering their low cost, hydrocyclones may be used together with other separation technologies. It would be especially beneficial to capture microplastic particles with a hydrocyclone prior to separation in a filtration unit, as this would reduce the problem of filter clogging.

Chapter 7

Discussion

This chapter will discuss the challenges encountered throughout the development of this project, as well as potential developments in the future.

As discussed in Chapter 5, the experiment was conducted before calibration of ViPA sensors. This resulted in some loss of data, as not all pictures of detected particles were saved. If a similar experiment was intended to be performed again, it would be beneficial to first calibrate the sensor based on the procedure proposed in Chapter 4.

Apart from adjustment of ESV and TV in microscopes, ViPA software allows for modification of DoF. In the proposed calibration procedure, DoF was fixed to the value which was previously used for calibration of these sensors for detection of oil droplets in water. DoF could be potentially adjusted, after selection of ESV and TV, to match the calculated concentration by ViPA software with the known true concentration. However, this would require additional precise offline sampling, to obtain information about the true concentration occurring in the calibration loop.

Obtained efficiencies from the main experiment could also be validated or compared with some form of offline concentration measurement. For instance, techniques such as μ FTIR Imaging or ATR-FTIR are available at AAU campus in Aalborg, and they could be used for the comparison. However, it is crucial to ensure that the validation measurement would be more reliable than online microscopy. Furthermore, uncertainties related to the unbiased extraction of samples from the setup should be eliminated.

In Chapter 5, the issue of additional and unwanted volume of water may be observed exiting through the overflow side. It was proposed to include Q_o or the flow split in the methodology of selecting the best operating conditions. Potentially, the additional dynamic microscope could be mounted on the overflow or overflow sidestream side to inform about the level of concentration of extracted mixture. However, it is important to consider the cost of additional ViPA sensor.

The majority of figures presented in Chapter 5 presented no significant difference between initial and best calibration settings in terms of observed concentration or efficiency. It could be questioned that due to this small difference in efficiencies at specific

segments, the proposed calibration procedure is unnecessary. Nevertheless, it is more reliable to trust calibration settings that were optimized, instead of arbitrarily selected values of ESV and TV .

The obtained efficiency was also presented as a function of Q_i and PDR . Therefore, a control algorithm could be designed in the future to maintain the high efficiency of microplastics separation inside the hydrocyclone.

Bibliography

- [1] Roland Geyer, Jenna R. Jambeck and Kara Lavender Law. 'Production, use, and fate of all plastics ever made'. en. In: *Science Advances* 3.7 (July 2017), e1700782. ISSN: 2375-2548. DOI: 10.1126/sciadv.1700782. URL: <https://www.science.org/doi/10.1126/sciadv.1700782> (visited on 02/05/2023).
- [2] Ben Mierement. *Addressing the challenge of Marine Plastic Litter using Circular Economy methods*. en. Tech. rep.
- [3] L. Lebreton et al. 'Evidence that the Great Pacific Garbage Patch is rapidly accumulating plastic'. en. In: *Scientific Reports* 8.1 (Mar. 2018), p. 4666. ISSN: 2045-2322. DOI: 10.1038/s41598-018-22939-w. URL: <https://www.nature.com/articles/s41598-018-22939-w> (visited on 03/05/2023).
- [4] Natalia P. Ivleva, Alexandra C. Wiesheu and Reinhard Niessner. 'Microplastic in Aquatic Ecosystems'. en. In: *Angewandte Chemie International Edition* 56.7 (Feb. 2017), pp. 1720–1739. ISSN: 14337851. DOI: 10.1002/anie.201606957. URL: <https://onlinelibrary.wiley.com/doi/10.1002/anie.201606957> (visited on 03/05/2023).
- [5] Bowen Li et al. 'Fish Ingest Microplastics Unintentionally'. In: *Environmental Science & Technology* 55.15 (Aug. 2021). Publisher: American Chemical Society, pp. 10471–10479. ISSN: 0013-936X. DOI: 10.1021/acs.est.1c01753. URL: <https://doi.org/10.1021/acs.est.1c01753> (visited on 04/05/2023).
- [6] Carolyn J. Foley et al. 'A meta-analysis of the effects of exposure to microplastics on fish and aquatic invertebrates'. en. In: *Science of The Total Environment* 631-632 (Aug. 2018), pp. 550–559. ISSN: 0048-9697. DOI: 10.1016/j.scitotenv.2018.03.046. URL: <https://www.sciencedirect.com/science/article/pii/S0048969718307630> (visited on 04/05/2023).
- [7] Sarah E. Nelms et al. 'Investigating microplastic trophic transfer in marine top predators'. en. In: *Environmental Pollution* 238 (July 2018), pp. 999–1007. ISSN: 02697491. DOI: 10.1016/j.envpol.2018.02.016. URL: <https://linkinghub.elsevier.com/retrieve/pii/S0269749117343294> (visited on 05/05/2023).

- [8] Junjie Zhang et al. 'Occurrence of Polyethylene Terephthalate and Polycarbonate Microplastics in Infant and Adult Feces'. In: *Environmental Science & Technology Letters* 8.11 (Nov. 2021). Publisher: American Chemical Society, pp. 989–994. DOI: 10.1021/acs.estlett.1c00559. URL: <https://doi.org/10.1021/acs.estlett.1c00559> (visited on 06/05/2023).
- [9] Nur Hazimah Mohamed Nor et al. 'Lifetime Accumulation of Microplastic in Children and Adults'. en. In: *Environmental Science & Technology* 55.8 (Apr. 2021), pp. 5084–5096. ISSN: 0013-936X, 1520-5851. DOI: 10.1021/acs.est.0c07384. URL: <https://pubs.acs.org/doi/10.1021/acs.est.0c07384> (visited on 06/05/2023).
- [10] Tan Suet May Amelia et al. 'Marine microplastics as vectors of major ocean pollutants and its hazards to the marine ecosystem and humans'. en. In: *Progress in Earth and Planetary Science* 8.1 (Jan. 2021), p. 12. ISSN: 2197-4284. DOI: 10.1186/s40645-020-00405-4. URL: <https://progearthplanetsci.springeropen.com/articles/10.1186/s40645-020-00405-4> (visited on 06/05/2023).
- [11] Joana Correia Prata et al. 'Methods for sampling and detection of microplastics in water and sediment: A critical review'. en. In: *TrAC Trends in Analytical Chemistry* 110 (Jan. 2019), pp. 150–159. ISSN: 01659936. DOI: 10.1016/j.trac.2018.10.029. URL: <https://linkinghub.elsevier.com/retrieve/pii/S0165993618305247> (visited on 19/05/2023).
- [12] H.A. Leslie et al. 'Microplastics en route: Field measurements in the Dutch river delta and Amsterdam canals, wastewater treatment plants, North Sea sediments and biota'. en. In: *Environment International* 101 (Apr. 2017), pp. 133–142. ISSN: 01604120. DOI: 10.1016/j.envint.2017.01.018. URL: <https://linkinghub.elsevier.com/retrieve/pii/S0160412017301654> (visited on 19/05/2023).
- [13] Riaz Ahmed et al. 'Critical review of microplastics removal from the environment'. en. In: *Chemosphere* 293 (Apr. 2022), p. 133557. ISSN: 00456535. DOI: 10.1016/j.chemosphere.2022.133557. URL: <https://linkinghub.elsevier.com/retrieve/pii/S0045653522000467> (visited on 19/05/2023).
- [14] Maocai Shen et al. 'Efficient removal of microplastics from wastewater by an electrocoagulation process'. en. In: *Chemical Engineering Journal* 428 (Jan. 2022), p. 131161. ISSN: 13858947. DOI: 10.1016/j.cej.2021.131161. URL: <https://linkinghub.elsevier.com/retrieve/pii/S138589472102742X> (visited on 19/05/2023).
- [15] Mohsen Padervand et al. 'Removal of microplastics from the environment. A review'. en. In: *Environmental Chemistry Letters* 18.3 (May 2020), pp. 807–828. ISSN: 1610-3661. DOI: 10.1007/s10311-020-00983-1. URL: <https://doi.org/10.1007/s10311-020-00983-1> (visited on 19/05/2023).

- [16] Petar Durdevic, Simon Pedersen and Zhenyu Yang. 'Challenges in Modelling and Control of Offshore De-oiling Hydrocyclone Systems'. In: *Journal of Physics: Conference Series* 783 (Jan. 2017), p. 012048. ISSN: 1742-6588, 1742-6596. DOI: 10.1088/1742-6596/783/1/012048. URL: <https://iopscience.iop.org/article/10.1088/1742-6596/783/1/012048> (visited on 18/05/2023).
- [17] Trygve Husveg et al. 'Performance of a deoiling hydrocyclone during variable flow rates'. en. In: *Minerals Engineering* 20.4 (Apr. 2007), pp. 368–379. ISSN: 08926875. DOI: 10.1016/j.mineng.2006.12.002. URL: <https://linkinghub.elsevier.com/retrieve/pii/S089268750600313X> (visited on 24/05/2023).
- [18] *Jorin ViPA Datasheet*. URL: <http://www.jorin.co.uk/wp-content/uploads/2020/12/Jorin-ViPA-B-HF.pdf>.
- [19] Dennis Severin Hansen et al. 'Offshore Online Measurements of Total Suspended Solids Using Microscopy Analyzers'. en. In: *Sensors* 21.9 (May 2021), p. 3192. ISSN: 1424-8220. DOI: 10.3390/s21093192. URL: <https://www.mdpi.com/1424-8220/21/9/3192> (visited on 21/05/2023).
- [20] Dennis Severin Hansen et al. 'Online Quality Measurements of Total Suspended Solids for Offshore Reinjection: A Review Study'. en. In: *Energies* 14.4 (Feb. 2021), p. 967. ISSN: 1996-1073. DOI: 10.3390/en14040967. URL: <https://www.mdpi.com/1996-1073/14/4/967> (visited on 24/05/2023).
- [21] *z-test - MATLAB ztest - MathWorks Nordic*. URL: <https://se.mathworks.com/help/stats/ztest.html> (visited on 14/04/2023).
- [22] Frank J. Massey. 'The Kolmogorov-Smirnov Test for Goodness of Fit'. en. In: *Journal of the American Statistical Association* 46.253 (Mar. 1951), pp. 68–78. ISSN: 0162-1459, 1537-274X. DOI: 10.1080/01621459.1951.10500769. URL: <http://www.tandfonline.com/doi/abs/10.1080/01621459.1951.10500769> (visited on 15/04/2023).
- [23] *Chi-square variance test - MATLAB vartest - MathWorks Nordic*. URL: <https://se.mathworks.com/help/stats/vartest.html> (visited on 26/04/2023).
- [24] David JC MacKay and David JC Mac Kay. *Information theory, inference and learning algorithms*. Cambridge university press, 2003.
- [25] S. Kullback and R. A. Leibler. 'On Information and Sufficiency'. In: *The Annals of Mathematical Statistics* 22.1 (Mar. 1951). Publisher: Institute of Mathematical Statistics, pp. 79–86. ISSN: 0003-4851, 2168-8990. DOI: 10.1214/aoms/1177729694. URL: <https://projecteuclid.org/journals/annals-of-mathematical-statistics/volume-22/issue-1/On-Information-and-Sufficiency/10.1214/aoms/1177729694.full> (visited on 26/04/2023).

- [26] B. Fuglede and F. Topsøe. 'Jensen-Shannon divergence and Hilbert space embedding'. en. In: *International Symposium on Information Theory, 2004. ISIT 2004. Proceedings*. Chicago, Illinois, USA: IEEE, 2004, pp. 30–30. ISBN: 978-0-7803-8280-0. DOI: 10.1109/ISIT.2004.1365067. URL: <http://ieeexplore.ieee.org/document/1365067/> (visited on 27/04/2023).
- [27] *Skewness - MATLAB skewness - MathWorks Nordic*. URL: <https://se.mathworks.com/help/stats/skewness.html> (visited on 28/04/2023).

Appendix A

Additional Plots

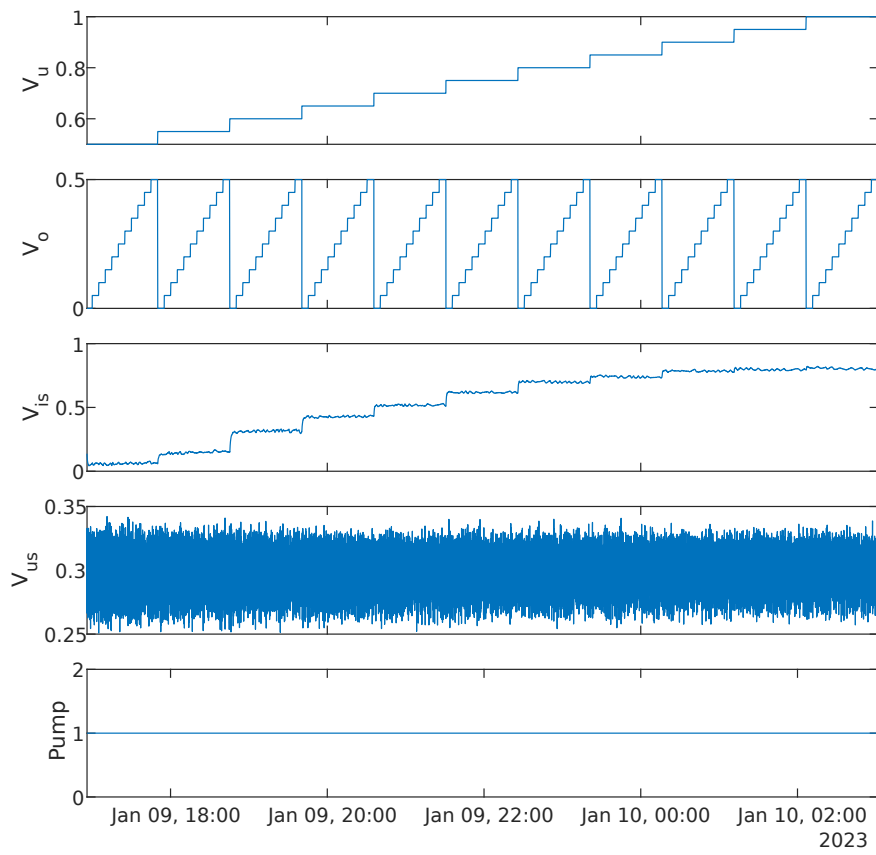


Figure A.1: All valve angles and pump signal

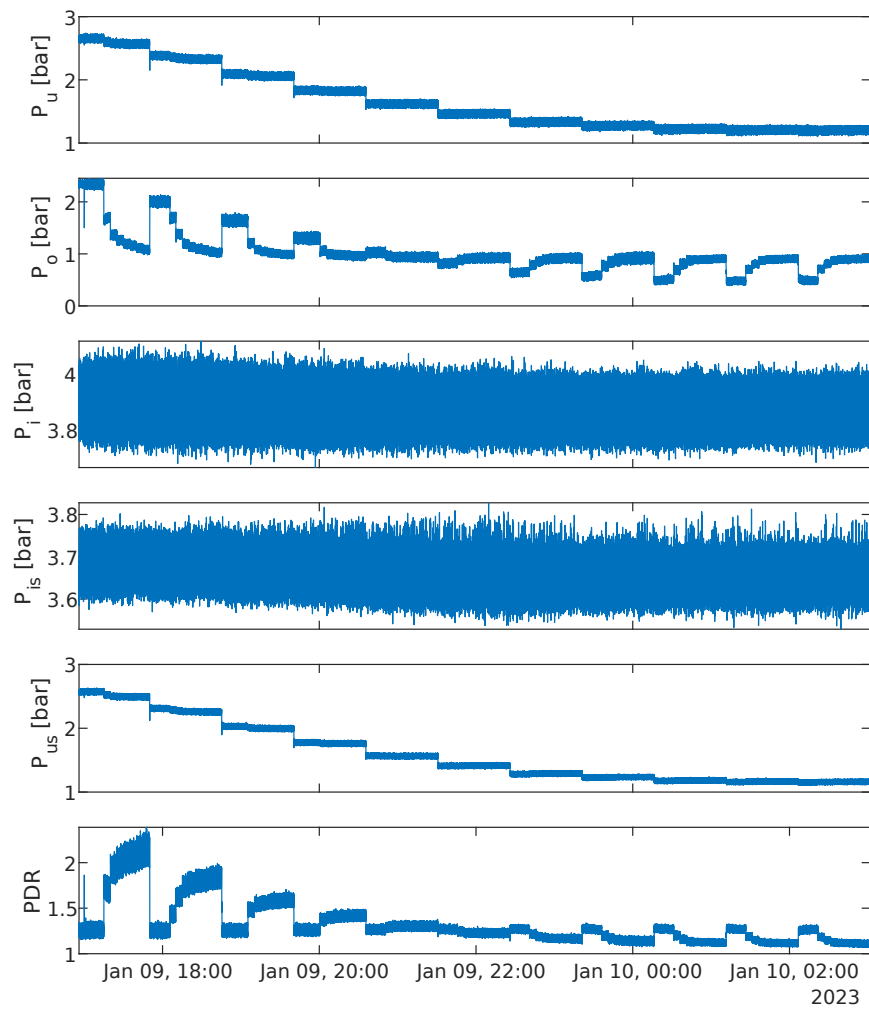


Figure A.2: All pressure signals

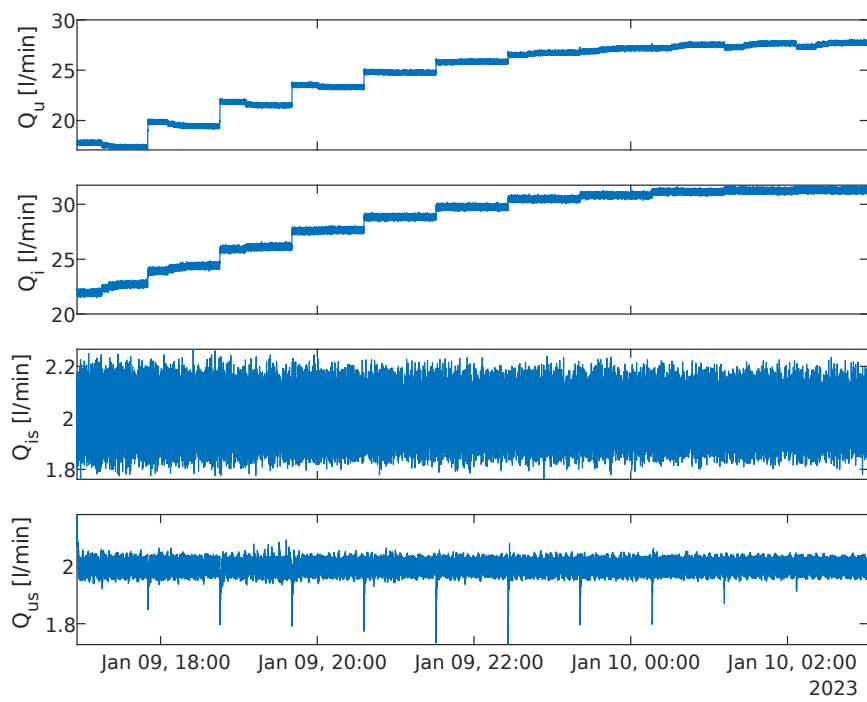


Figure A.3: All flow rate signals

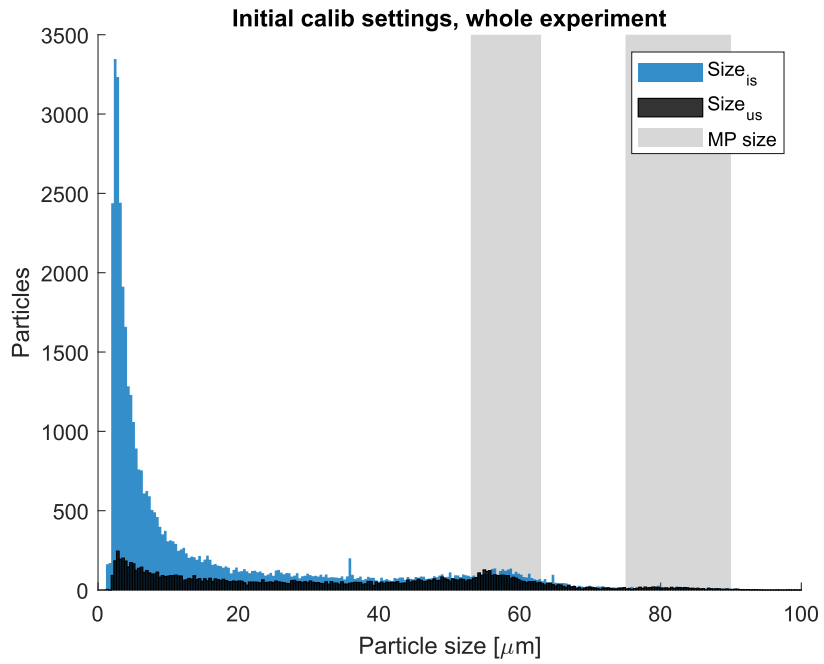


Figure A.4: Histogram of all detected particles for initial calibration settings

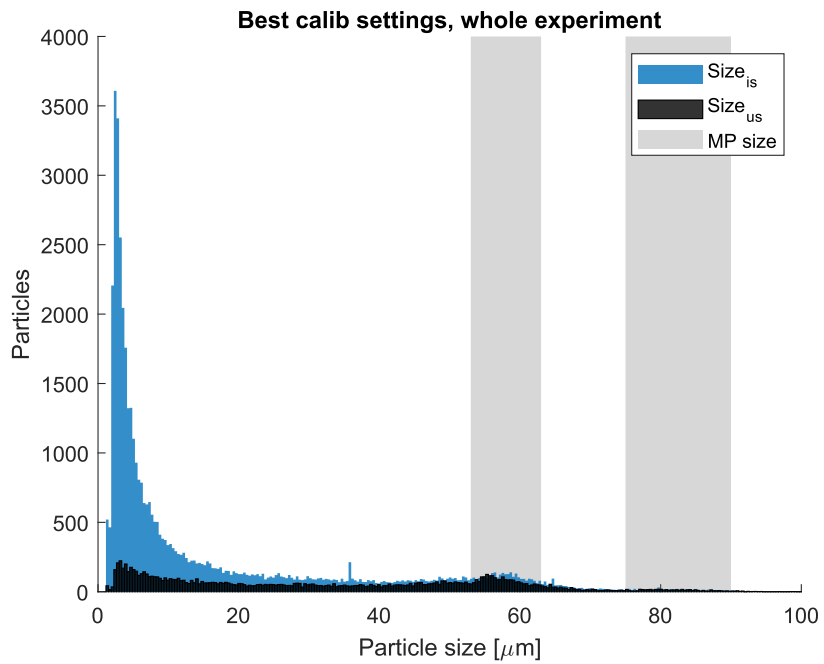


Figure A.5: Histogram of all detected particles for best calibration settings